UNIVERSITAT POLITÈCNICA DE CATALUNYA
BARCELONATECH

MASTER THESIS

Fluidic oscillators: decoupling amplitude and frequency

Aleix Calderón Usán

SUPERVISED BY

Fernando Mellibovsky Elstein

Universitat Politècnica de Catalunya
Master in Aerospace Science & Technology
September 2018

Fluidic oscillators: decoupling amplitude and frequency

BY

Aleix Calderón Usán

DIPLOMA THESIS FOR DEGREE

Master in Aerospace Science and Technology

AT

Universitat Politècnica de Catalunya

SUPERVISED BY

Fernando Mellibovsky Elstein

Physics Department

Abstract

The purpose of this thesis is to find a way to decouple the amplitude and the frequency of the oscillatory jet in the output of a fluidic oscillator by modifying a geometrical parameter and the Reynolds number, with the assistance of computational fluid dynamics (CFD). Fluidic oscillators are a type of active flow control that can be used to delay boundary layer separation, a problem that arises in aircraft wings when facing the airstream at a high angle of attack that causes a sudden decrease in lift and a high increase in drag. Fluidic oscillators improve this situation by injecting an oscillatory jet into the boundary layer, which converts the boundary layer into a turbulent one that can stay attached to the wing for longer. The advantage of the fluidic oscillator with respect to other active flow control devices is that, in its core design, it contains no moving parts, making it more robust than the rest. The version of the fluidic oscillator used in this study has been simplified with the design target of having a geometric parameter that can be modified during operation. The results focus on the internal dynamics of the fluidic oscillator and in the dependence of the amplitude and the frequency with respect to the Reynolds number and the geometric parameter, both separately and together. They show that the amplitude and frequency increase and decrease, respectively, with both an increasing Reynolds number and an increasing geometric parameter, within the operational range of the fluidic oscillator. This allows for both parameters to be modified independently but in limited increments, due to the similar behavior between changing the Reynolds number and the geometric parameter.

Contents

List of Figures

List of Tables

1 Introduction

Plenty of research is being performed on the topic of boundary layer control, some of which is centered around flow control in the wings of aircraft, but not exclusively to that field. Specifically, active flow control methods are gaining popularity due to the benefits they present with respect to their passive counterparts.

Of the set of existing active flow control devices, the one studied in this thesis is the fluidic oscillator, a very promising active flow control device which stands out from the rest due to its simplicity. It works by converting a pressurized jet into an oscillatory one as a result of its inner geometry only, and its output frequency and amplitude depend on the flow rate of the fluid.

The objective of this thesis is to study the possibility of tweaking the amplitude and frequency of the output of the fluidic oscillator independently when the flow rate changes by the means of modifying its geometry, to determine if it's possible to extend the functionality of the device to multiple stages while in operation. A secondary objective that will lead to the accomplishment of the main one is to better understand how fluidic oscillators work and how they react to changes such as in the flow rate and in their geometry.

In order to pursue the set objectives, computational fluid dynamics techniques will be used to simulate the behavior of the fluidic oscillator under several different circumstances. The data obtained from the simulations will then be analyzed to quantify the results and help explain any phenomena that may arise.

The structure of the text will be as follows: in the first section, a brief introduction to appreciate the importance of boundary layer control will be given, followed by an overview of the state of the art in flow control actuators, both passive and active. Among them, the fluidic oscillator will be explained in much more detail, providing a basis which will help explain the rest of the thesis.

After that, the newly designed simpler geometry of the fluidic oscillator that will be used for the simulations will be defined. This new design allows to change the geometry during operation according to the specific requirements that may appear. Two different designs with a slight change between them will be proposed.

Then, everything needed in order to perform the simulations will be described: first, a brief overview on the fundamental fluid dynamics governing equations will be given, and after that all the parameters that need to be set in order for the simulations to work will be fixed. This includes, for example, all the boundary conditions and the initial conditions for the simulations. Lastly, the process used to design the mesh of the fluidic oscillator and the time discretization method will be

explained, and the procedure used to process the outputs of the simulations will be presented.

Finally, several different simulations will be done in order to obtain the results. The first simulations that need to be done are those to compare the two different geometries, in order to decide which design will be used for the subsequent simulations. With the simulation performed with the chosen design, the internal dynamics of the fluidic oscillator will be studied in much more detail, providing a foundation that will be used to better understand the phenomena that will be encountered in the final simulations. Then, the effects in the amplitude and the frequency caused by a change in the flow rate or a change in the geometry of the fluidic oscillator will be studied. With the information gathered from that and from more simulations taken at different pairs of values of the flow rate and the geometric parameter, the response of the fluidic oscillator will be analyzed in different configurations, in order to determine how the amplitude and the frequency can be modified independently.

2 Background

2.1 The problem of boundary layer separation in airfoils

Even though real fluids feel friction forces due to their viscosity, at a high enough velocity they can behave almost as ideal fluids in some regions, except within a thin layer around any object submerged in the fluid, called the boundary layer. In this thin region, the effects of viscosity are much more noticeable due to the interactions between the fluid particles and the object walls which, in turn, cause the no slip condition. This condition states that for any fluid moving past an object, the relative velocity of the fluid layer touching the object must be zero. As a consequence, considerable shearing forces are present in the boundary layer, even for low viscosity fluids, due to the large velocity gradients present near the object surfaces, as seen in Fig. 1.

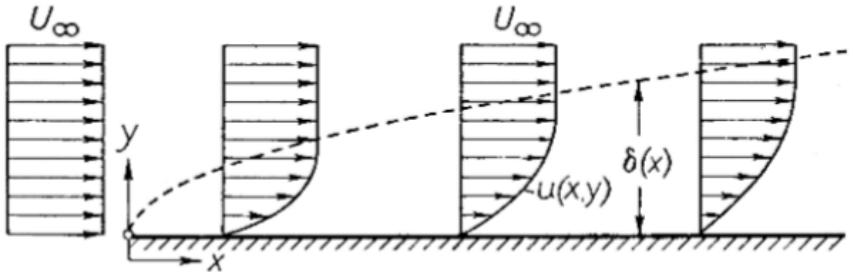

Figure 1: Graphical depiction of the boundary layer near a solid wall. Extracted from [12].

The boundary layer is especially important in the case of the wings of airplanes, since it determines the path the air will follow around it. At low angles of attack, the boundary layer is very thin, and therefore doesn't influence very much the path followed by the air. Therefore, in this case, the air follows the shape of the airfoil with little perturbation. However, as the angle of attack increases, the boundary layer increases in size, until the point in which it detaches from the airfoil, and the airflow changes the path it follows drastically, as can be seen in Fig. 2, consequently losing the aerodynamic capabilities of the airfoil and therefore increasing drag dramatically and decreasing lift.

2.2 Boundary layer control

Due to the huge complications boundary layer separation brings, much effort has been devoted into finding ways to delay the separation as much as possible, allowing aircraft to achieve higher angles of attack, diminishing parasitic drag and reducing the risk of stall.

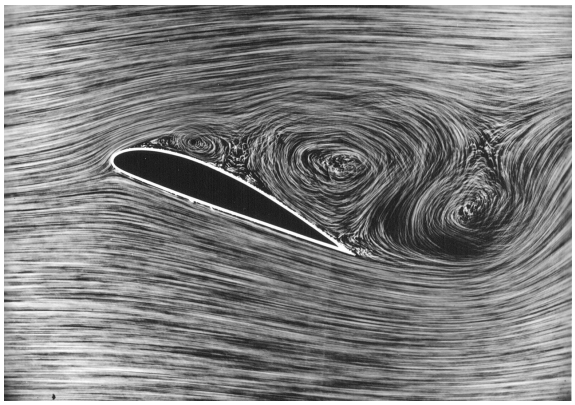

Figure 2: Boundary layer separation in an airfoil at a high angle of attack. Extracted from [18].

The most commonly used apparatus for boundary layer control are passive flow control devices. These, in one way or another, help the boundary layer to attach to the object without the need of any active intervention. The most widely used passive flow control devices are vortex generators. Vortex generators are little vanes placed near the leading edge of the aircraft wings which create small vortices that convert the boundary layer from laminar to turbulent. This energizes the boundary layer, and the extra momentum induced into it prevents the separation from occurring.

However, even though passive flow control devices are beneficial for boundary layer control, they also have their inconveniences. Due to the fact that they are passive, they actuate when they are required but also when they are not. For example, in the case of vortex generators, cruise speed may be reduced slightly due to the increased drag, while in this scenario they serve very little purpose since the angle of attack is minimal.

This is the main reason why active flow control devices are being developed. They provide the benefits of passive control devices when they are required, but they can also be turned off when they are not needed. The first active flow control devices to be proposed worked by blowing or suction.

The first method devised to control separation was by suction. Since one of the causes of boundary layer separation is the reduction of momentum near the airfoil structure, this method works by removing the low momentum fluid present in the boundary layer, giving space to more energetic fluid which can stay attached to the surface for longer. This has been proven to work well using mock-ups in wind tunnels and even in some experimental aircraft, but due to the mechanical complexity of the components and the added weight, the benefits don't really compensate for the inconveniences.

There are also flow control methods by steady blowing. The reasoning behind these methods is that adding momentum to the decelerated airflow near the surface

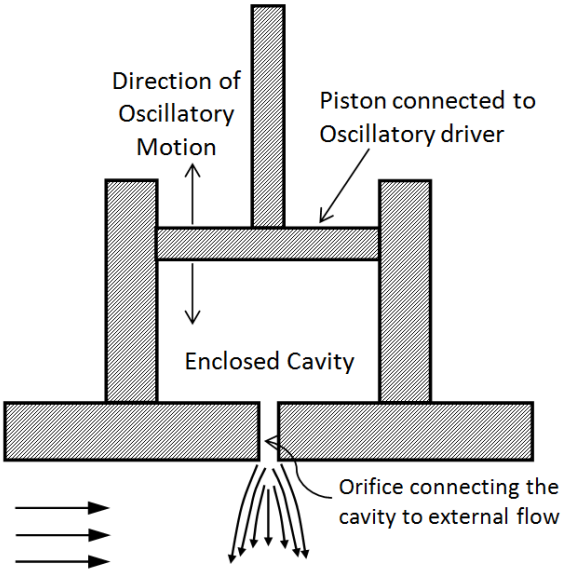

Figure 3: Diagram of a synthetic jet actuator. Extracted from [10].

of the airfoil will delay separation. This can be achieved by actively blowing air from a compressor, or by passively redirecting airflow from a different part of the airfoil to the desired place. However, it has been shown that periodic addition of momentum can help reduce boundary layer separation better than steady blowing.

Some examples of more advanced active flow control devices are the following:

- Synthetic jet actuators: they work by suctioning and blowing the fluid periodically by having an oscillating piston (as shown on Fig. 3) or diaphragm expanding and contracting a cavity situated in contact with the surface. They are also called zero-net mass-flux (ZNMF) actuators, since in average they don't provide any mass injection to the boundary layer, but they do in turn add momentum to it.

- Plasma actuators: they consist of an electrode in contact with the airflow separated of another electrode covered by a piece of dielectric material and offset in the flow direction, as can be seen in Fig. 4. The encapsulated electrode is connected to ground, while the exposed electrode is provided a high voltage, which creates a plasma flow going in the airstream direction, between the two electrodes. This plasma flow is accelerated due to the difference in potential between the electrodes, and in turn it accelerates the neutrally charged fluid, energizing the boundary layer and preventing separation. One of the main benefits of this kind of actuator is that it doesn't contain any moving parts.

- Pulsed jets: they apply a pulsating mass flow to the boundary layer by expelling fluid through a nozzle. This pulsed jet can be produced either mechanically, electrically or through combustion (by igniting gaseous fuel and

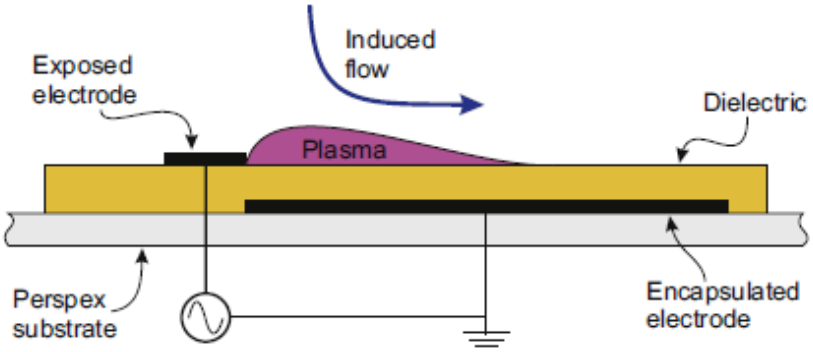

Figure 4: Diagram of a plasma actuator. Extracted from [6].

oxidizer in an small combustion chamber). These devices, unlike synthetic jet actuators, offer a non-zero net mass flux, at the cost of requiring an external fluid or fuel source in order to operate.

- Piezoelectric flaps: piezoelectric flaps are cantilever beams that can vibrate when an AC voltage is applied. The vibration then interacts with the boundary layer.

- Active dimples: they actuate as on-demand vortex generators by using electro-active polymers which, when applied an electromagnetic field, shrink, roughening the surface and generating a turbulent boundary layer, similarly to a golf ball's dimples.

- Fluidic oscillators: due to the inner workings of fluidic oscillators, which will be explained more in detail in the following sections, fluidic oscillators can convert a pressurized flow of fluid into an oscillatory jet (or a pulsating jet, if the output is divided in two with a wedge) without the need of any movable parts. By injecting the oscillatory or pulsating jet into the boundary layer, it energizes it and delays boundary layer separation.

2.3 The fluidic oscillator

A fluidic oscillator consists of an inlet nozzle through which the pressurized jet enters the system, the mixing chamber, placed in the middle of the two inner blocks, the two feedback channels which connect the end of the mixing chamber to its beginning, and the outlet nozzle, placed at the end of the mixing chamber and letting the jet go outside. These parts can be identified in Fig. 5.

Fluidic oscillators produce an oscillating jet from a pressurized stationary flow as a result of the internal instabilities of the flow through its geometry. The principal

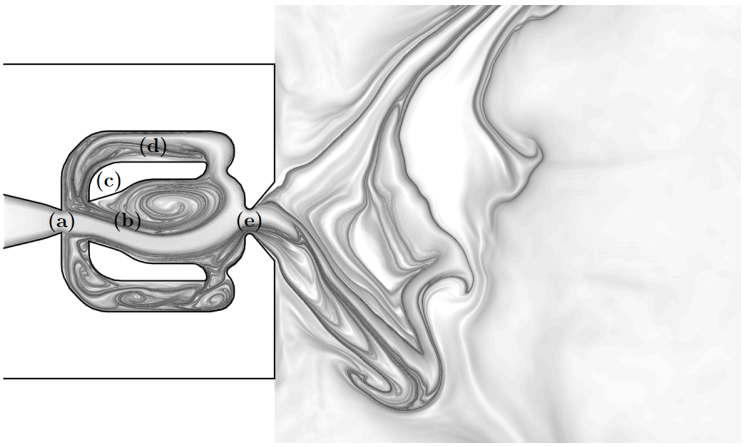

Figure 5: Flow inside a fluidic oscillator, with the structures formed by the flow depicted with the finite-time Lyapunov exponent. Its constituent parts are (a) the inlet nozzle, (b) the mixing chamber, (c) the inner blocks, (d) the feedback channels and (e) the outlet nozzle. Extracted from [13].

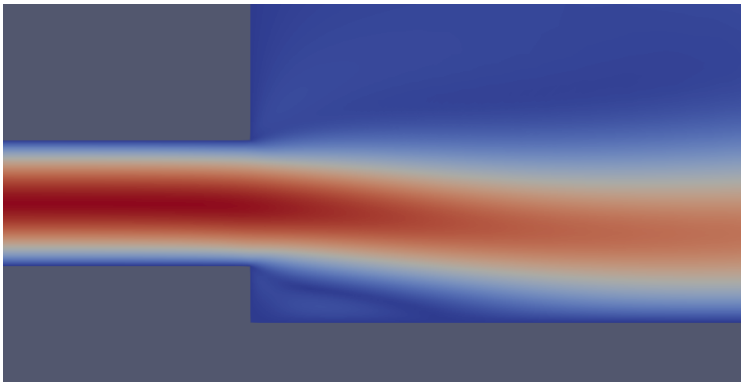

Figure 6: Simulation depicting the attachment of a jet to a wall due to the Coandă effect.

cause of the internal instabilities that produce the oscillatory motion is the Coandă effect.

The Coandă effect is the propensity of a fluid jet to attach and stay adhered to any surface. When a jet of fluid advances, it creates an area of low pressure on all sides around itself. When the jet is unrestrained, the force exerted on it by the ambient pressure compensates in all directions, so the jet follows a straight line. However, if there is a restriction in one of the sides such as a wall, there will be a pressure difference between the low pressure area near the wall and the ambient pressure on the opposite side, which will create a net force on the jet towards the wall. This force then pushes the jet until it reaches equilibrium flowing attached to the wall. This situation can be visualized in Fig. 6.

In the case of the fluidic oscillator, when the jet enters the mixing chamber the situation is symmetric and there are low pressure areas on both the bottom and top of the jet, so the jet should stay straight. However, at a sufficiently high flow rate, any small perturbation in the jet within the mixing chamber can push the jet to one

side or the other and, at that point, the Coandă effect attaches the jet towards one of the walls of the inner blocks. Due to the flow geometry, the jet exits the outlet nozzle at an angle, as can be seen in Fig. 5.

The jet would remain stably attached to the wall if there weren't any feedback channels. However, due to their presence and the geometry of the outlet nozzle, part of the jet is deflected to the feedback channel, which reenters the beginning of the mixing chamber with relatively low momentum, generating a recirculation bubble between the jet and the wall that pushes the jet towards the opposite wall, completing one semicycle. The same process is then repeated in the other side, maintaining the oscillation of the jet outside the outlet nozzle.

The inner dynamics of the fluidic oscillator and the mechanism that drives the oscillatory motion will be discussed in further depth in Sec. 5.2 with the aid of computer simulated results.

The frequency and the amplitude of the oscillating jet at the output generally depend on the input flow rate (or, more specifically, on the Reynolds number, which will be defined later), but it can also be affected by the geometry. The effects generated by the change in both of these parameters will be studied in detail in Sec. 5.

3 Design of the fluidic oscillator

Since both the oscillation frequency and the amplitude of the jet emerging from the fluidic oscillator are directly related to the flow rate, which is the sole actuation parameter, both of them are coupled in the original design of the fluidic oscillator, such as the one presented in Fig. 5. It would be desirable to decouple the two parameters, in order to obtain different amplitudes at any given frequency or vice versa.

One of the ways of modifying them for each flow rate value is to somehow modify the geometry of the fluidic oscillator. By changing the inner structure of the fluidic oscillator, such as the shape and length of the feedback channels, the shape of the inner blocks or the overall size of the device, the flow dynamics can change leading to a variation in frequency. However, the possible geometry modifications that can be applied to an already manufactured fluidic oscillator are restricted due to the fact that materials need to be rigid.

Therefore, in order to attain a situation where the geometry of the device can be modified at any time, and given that only translation and rotation of the internal components can be applied, the fluidic oscillator devised to be studied in this thesis has been redesigned to allow the inner blocks to move in a circular motion around the center of the oscillator, with the objective of being able to adapt its frequency and and output amplitude independently, according to the particular requirements, which might evolve during operation.

To facilitate the implementation of the moving inner blocks, they have been redesigned together with the overall shape of the fluidic oscillator, resulting in a change in the shape of the feedback channels and the mixing chamber. The result is a simplified version of the original fluidic oscillator that still maintains the most essential features required for the oscillatory motion to take place. This simplification of the geometry also allows to easily study the impact of any design changes towards the nature of the flow inside the fluidic oscillator.

It must be stated that the study performed in this thesis will be about a two-dimensional fluidic oscillator, neglecting the effects that the width may bring in a real three-dimensional structure.

3.1 Geometry

Two different geometries for the inner blocks have been designed for the purpose of this study:

The first one, shown in Fig. 7a, is a very simplistic approach that retains the basic features required for a fluidic oscillator to work while keeping a very simple geometry. The body of the fluidic oscillator is a circumference of radius R in which two opposite sides (in the case of the image, in the left and right) have been perforated to behave as the inlet and outlet nozzles, with a length of L_i and L_o and half-height of h_i and h_o, respectively. The latter extends outside the main body of the fluidic oscillator at a sharp angle defined as α. Within the outer circle lay the inner blocks, whose outer wall is shaped as a circumference of radius r concentric to the outer one which has been cut along two circumference chords, symmetric with respect to the horizontal axis, to form the inner walls. The two points that determine the vertices of the inner blocks (and therefore the chords that form the inner walls) are given by the angular distance φ between the line that connects them and the center of the fluidic oscillator and the symmetry axis of each block, which in turn is positioned by its angle θ from the vertical line.

The angle φ determines the size of the blocks together with the inner circumference radius r, while the angle θ determines their position, which can move around the center of the system, in a way so that when set to zero the inner walls become horizontal.

On the other hand, the second design, shown in Fig 7b, while very similar to the former in terms of general shape, features different inner blocks with a slightly more complex geometry, in order to further resemble the original design. The outer wall is equal to the one on the first design, but the inner wall is divided in two separate walls at an angle from each other. Thanks to this fact, the initial angle of the wall with respect to the horizontal is much sharper, which promotes easier detachment of the jet, and the remaining part of the inner wall can be at a shallower angle. Finally, the angular distance between the line that connects the center of the fluidic oscillator and the vertex between the two inner walls and the midpoint of the outer wall is determined by ψ, and the actual distance between the vertex and the outer wall is given by d_v.

The parameters d_v and ψ can be tweaked to allow the shallow part of the inner block's inner walls to be horizontal when the blocks are at a given angle $\theta_{default}$ from the vertical using the expression

$$d_v = r\left(\frac{\sin\left(\frac{\pi}{2}\right) - \theta_{default} - \varphi}{\sin\left(\frac{\pi}{2}\right) + \theta_{default} + \varphi} + 1\right), \tag{1}$$

which can be used to define the default position of the fluidic oscillator for any given φ.

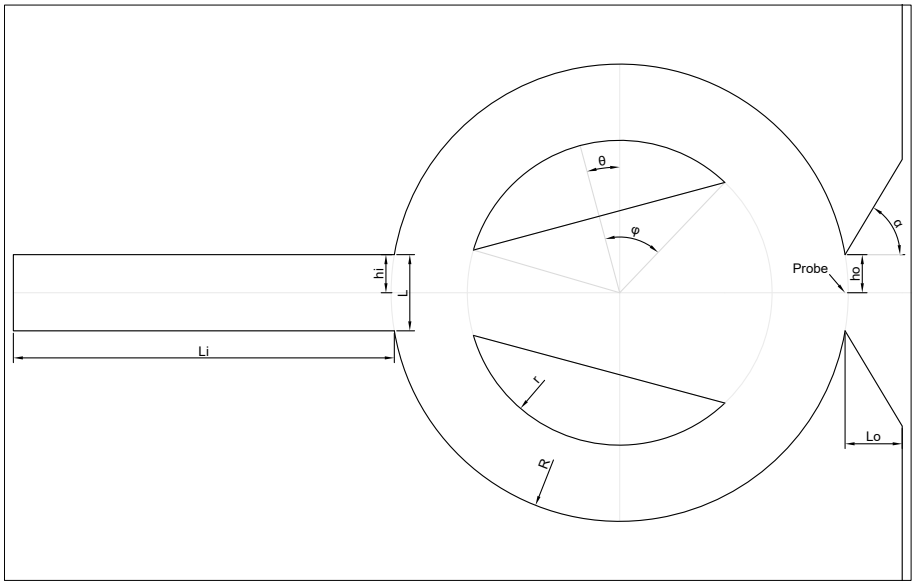

(a)

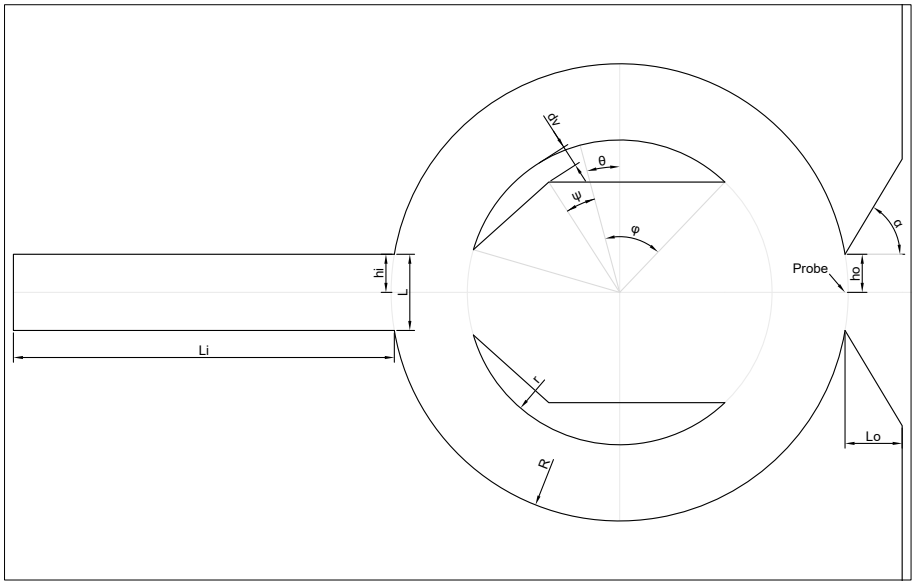

(b)

Figure 7: Sketch with the dimensions of (a) the first and (b) the second designs of the fluidic oscillator. The probe used later for the results is also shown.

Parameter	Value
L_i	7.5
h_i	0.5
L_o	0.75
h_o	0.5
α	$\frac{\pi}{3}$
R	3
r	2
φ	$2.02 \cdot \frac{\pi}{3}$
ψ	$1.75 \cdot \frac{\pi}{18}$
d_v	0.2884

Table 1: Dimensions of the base fluidic oscillator. Length parameters are stated in dimensionless units using the scaling factor $\frac{1}{2h_i}$ and angles are expressed in radians. The parameters ψ and d_v are only used for the second design. The value of d_v has been calculated using Eq. (1) so that the default position of the inner blocks (when the shallow part of the inner wall is horizontal) is at $\theta = 1.5 \cdot \frac{\pi}{18}$.

Taking all of the above into consideration, the dimensions of the base fluidic oscillator, designed so that its default inner block configuration is when $\theta_{default} = 1.5 \cdot \frac{\pi}{18}$, have been set to the values stated in Tab. 1, which correspond to the dimensions of the designs shown previously in Fig. 7. All parameters are scaled around the preset value of $h_i = 0.5$, so that $L = 2h_i$, the characteristic length of the system defined to be the height of the inlet nozzle, is normalized (i.e. $L = 1$).

Finally, as a side note, in both designs the optional splitter in the outlet nozzle that would turn the flow from oscillatory to pulsating has been omitted, since the interest of this thesis is mainly to study the internal fluid dynamics of the fluidic oscillator and their effect on the immediate output (the outlet nozzle), and little focus is put on its effects on the outside region. While the splitter may modify slightly the internal flow, its influence is supposed be minimal since all the phenomena that cause the oscillatory motion happen due to the influence of the flow with the internal geometry.

4 Solution approach

The dynamics of the flow inside the fluidic oscillators studied in this thesis have been determined with the aid of computational fluid dynamics (CFD). CFD methods use numerical approaches to solve the fluid dynamics governing equations in order to get the behavior of the fluid motion in systems with a geometry that doesn't allow an analytical solution.

Some assumptions will be made on the type of fluid used in the simulations: the fluidic oscillator will be submerged in a continuous medium of incompressible Newtonian fluid. This means that the density of the fluid is constant and that the viscosity is not dependent on the shear rate. External body forces such as gravity will be omitted.

4.1 Fluid dynamics governing equations

The motion of fluids is governed mainly by three different equations that represent, respectively, the conservation of mass, the conservation of momentum and the conservation of energy. However, the latter decouples for incompressible flow in the absence of thermal effects.

The equation that describes the conservation of mass is the continuity equation

$$\underbrace{\frac{\partial \rho}{\partial t}}_{I} + \underbrace{\vec{\nabla} \cdot (\rho \vec{u})}_{II} = 0\,, \tag{2}$$

where ρ is the density of the fluid. In the equation, I indicates the temporal variation of the total mass (per unit volume) of the system and II states the difference between the incoming and the outgoing flow. What this means is that any increase (or decrease) in mass is caused by the fact that different amounts of fluid enter and leave the system.

In the case of an incompressible flow, where ρ remains constant, the first term of Eq. (2) vanishes and the equation becomes

$$\vec{\nabla} \cdot \vec{u} = 0\,, \tag{3}$$

which states that the amount of incoming fluid must be equal to the fluid that exits the system.

The conservation of momentum is described by the Navier-Stokes equations, which describe the motion of fluids in which the viscosity is non-zero. For Newtonian

incompressible flows without the influence of gravity, it is given by

$$\underbrace{\frac{\partial \vec{u}}{\partial t}}_{I} + \underbrace{\left(\vec{u}\cdot\vec{\nabla}\right)\vec{u}}_{II} = \underbrace{-\frac{1}{\rho}\vec{\nabla}P}_{III} + \underbrace{\nu\nabla^2\vec{u}}_{IV}, \tag{4}$$

where I indicates the temporal variation of the velocity, II is the convection term, III is the force due to the pressure, which promotes the motion and IV represents the diffusion. The term ν is the kinematic viscosity, which is defined as the quotient between the viscosity of the fluid μ and the density:

$$\nu = \frac{\mu}{\rho}\,. \tag{5}$$

4.2 Setting up the simulation environment

As stated at the beginning of Sec. 4, the governing equations of motion cannot be solved analytically for all geometries. In these cases, CFD methods must be used in order to obtain the fluid flow status at each point in space and time. The software used to solve Eqs. (2) and (4) is Nektar++, which allows to solve several partial differential equations using the spectral/hp element method.

In order to facilitate the setup of the simulations, the mean velocity emerging from the inlet nozzle has been set to $u_{mean} = 1$ in dimensionless units. This, together with the fact that the dimensions of the fluidic oscillator have been normalized so that the characteristic length is $L = 1$, as explained in Sec. 3.1, results in the Reynolds number, which is defined as

$$Re = \frac{uL}{\nu}\,, \tag{6}$$

to become

$$Re = \frac{1}{\nu}\,. \tag{7}$$

Also, the density is set to $\rho = 1$. Taking this into account and the relation between the Reynolds number and the kinematic viscosity stated in Eq. (7), the Navier-Stokes equation can be nondimensionalized to

$$\frac{\partial \vec{u}}{\partial t} + \left(\vec{u}\cdot\vec{\nabla}\right)\vec{u} = -\vec{\nabla}P + \frac{1}{Re}\nabla^2\vec{u}\,, \tag{8}$$

where the only parameter that can be changed is the Reynolds number.

To solve the fluid governing equations, the boundary conditions for all the contours of the system must be preset to values which are known and determined. As

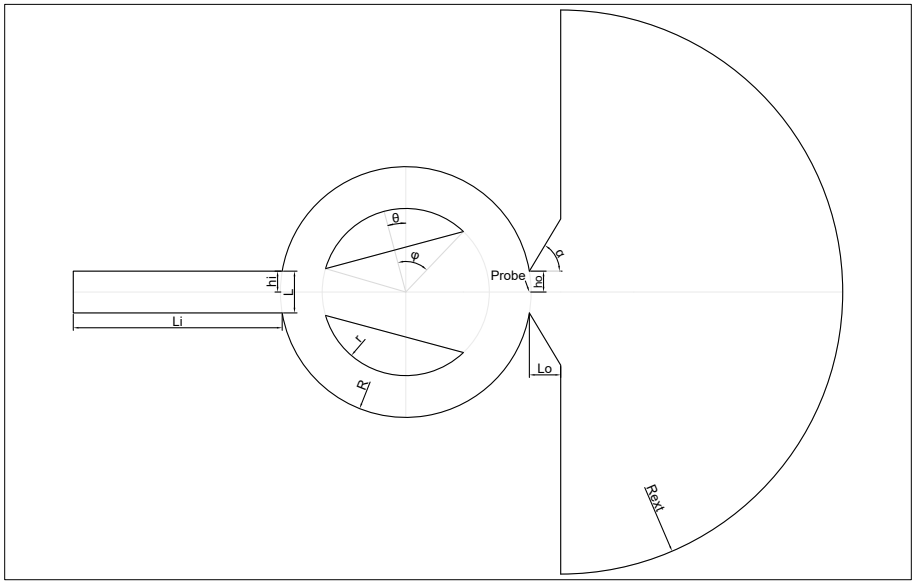

Figure 8: Sketch with the full geometry to be simulated, including the outer region, of the first design of the fluidic oscillator (the outer region is identical for the second design). The probe used later for the results is also shown. The outer region radius is not to scale.

a consequence, there cannot be any openings in the area to solve (such as the outlet nozzle), so an outlet region with an outflow contour must be attached to the fluidic oscillator in order to enclose the simulated area. This outer region must be big enough so that it doesn't interfere with the inner dynamics, and so that it can be interpreted as an open outside region.

The design of the fluidic oscillator with an added semicircular outer region of radius R_{ext} can be seen in Fig. 8. The size of this outer region has been set to $R_{ext} = 50$, an order of magnitude higher than the rest of the dimensions stated in Tab. 1.

In all the different contours, three different boundary conditions have been used for the fluid governing equations:

- Dirichlet boundary conditions: the value that the solution must have along the boundary $\partial\Omega$ is set to the appropriate value, so that

$$q\left(x\right)|_{\partial\Omega} = f\left(x\right) \ . \tag{9}$$

- Neumann boundary conditions: the value of the derivative of the solution along the boundary $\partial\Omega$ is set to the appropriate value, so that

$$\frac{\partial q}{\partial \vec{n}}\left(x\right)\Big|_{\partial\Omega} = f\left(x\right) \ , \tag{10}$$

where $\vec{n}$ is the normal direction to the boundary $\partial\Omega$.

- Robin boundary conditions: a linear combination of the solution and its derivative is set to a given value, so that

$$\beta q\left(x\right) + \frac{\partial q}{\partial \vec{n}}\left(x\right)\Big|_{\partial\Omega} = f\left(x\right) . \tag{11}$$

  They can be considered a weighted combination of Dirichlet and Neumann boundary conditions, where β is the weighting coefficient.

In the inlet, which can be considered a tube of length greater than it's width, the solution is known to be a Poiseuille flow, which states that the velocity profile along the width of the tube has to be a symmetric parabola with respect to the center of the tube with a value of zero in the walls, due to the no slip condition. Given that the velocity profile has been set so that the mean velocity is $u_{mean} = 1$, the resulting velocity profile has to be

$$u\left(y\right) = \frac{3}{2}\left(1 - \left(\frac{y}{h_i}\right)^2\right) . \tag{12}$$

This value, which is dependent on the distance y from the x-axis, has been set as a Dirichlet boundary condition in the beginning of the inlet nozzle for the horizontal velocity u, together with a value of $v = 0$ for its vertical component. The value of the pressure is not known, but its derivative can be set to zero, so a Neumann boundary condition for the pressure has been set in the inlet so that $\frac{\partial p}{\partial x} = 0$. The actual boundary conditions used for the pressure are high-order Neumann boundary conditions, which also consider higher order derivatives.

In the rest of physical walls of the fluidic oscillator, both the horizontal and vertical components of the velocity must be zero due to the no slip condition, so these values have been set as Dirichlet boundary conditions. The pressure boundary condition in these walls has also been set to a Neumann boundary condition with value zero.

Finally, the outflow semicircular contour at the end of the outlet region has been set with Robin boundary conditions for the two components of the velocity and the pressure to allow them to dissipate once the flow from the fluidic oscillator arrives at this boundary. The values for these boundary conditions are set to $f\left(x\right) = 0$, and the weighting coefficients to $\beta_{u,v} = \frac{D_0}{\Delta t}$ and $\beta_p = \frac{1}{D_0 \nu}$ for the velocity and the pressure conditions, respectively[1], where D_0 is a non-negative constant (set to $D_0 = 1$ in this case) and Δt is the time step, described later in Sec. 4.3.

[1]These values are set according to the formulation developed in "A convective-like energy-stable open boundary condition for simulations of incompressible flows", by S. Dong, Journal of Computational Physics, 2015.

Before using the Robin boundary conditions, Neumann ones for the velocity and Dirichlet for the pressure were considered, but they were disregarded since they caused instabilities in the simulations once the jet arrived at the outflow boundary. Robin boundary conditions can be used in Nektar++ in a way that allows implementing accurate convective-type outflow boundary conditions, which prevent the kinetic energy of the outgoing vortices to be reflected back into the domain.

Apart from the boundary conditions, an initial value of the solution must be set in the whole domain. For the first simulations, the initial conditions have been set to those of a stationary fluid ($u = 0$, $v = 0$ and $p = 0$), but with a slight perturbation in the velocity field in the form of a random value three orders of magnitude lower than the mean velocity of the jet in the inlet, in order to facilitate the initial perturbation that eventually leads to the oscillatory mechanism. In later simulations, the initial conditions have been set to an already oscillating solution, in which the transient phase has already been overcome.

4.3 Time and space discretization

The strategy used to solve the equations numerically is to discretize both time and space instead of solving them for a continuous domain.

For the time dimension, the solver integrates the governing equations using a Velocity Correction Scheme of order 4, which decouples the pressure and velocity so that they can be handled separately, over time in little time steps Δt, taking a previous state and modifying it according to the equations. The time step for the simulations has been set to $\Delta t = 0.002$, in dimensionless units.

For the space dimension, the domain is subdivided in a grid with many elements called a mesh. The equations are expressed in their weak form and discretized using the spectral element method. Ideally, a mesh would contain infinitesimally close elements, but that would be impossible to simulate. Therefore, a good compromise between good accuracy and keeping the computation time relatively low must be taken. This is achieved by a careful design of the mesh which contains many elements close together in areas where the flow is complex (such as near walls and corners) but fewer elements in areas with little change.

For the simulations in this thesis, a structured mesh comprised of quadrilaterals has been chosen, instead of an unstructured mesh composed of irregular shapes. These are more difficult to obtain (and in some occasions impossible), but they are preferred in situations where the flow orientation can be predicted. To design a structured mesh, the whole domain is first divided into smaller surfaces, as can

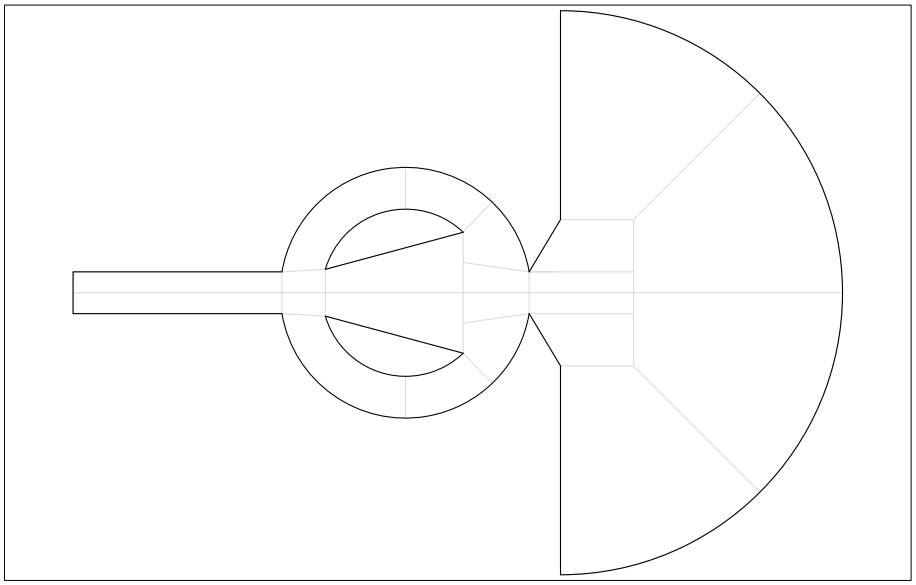

(a)

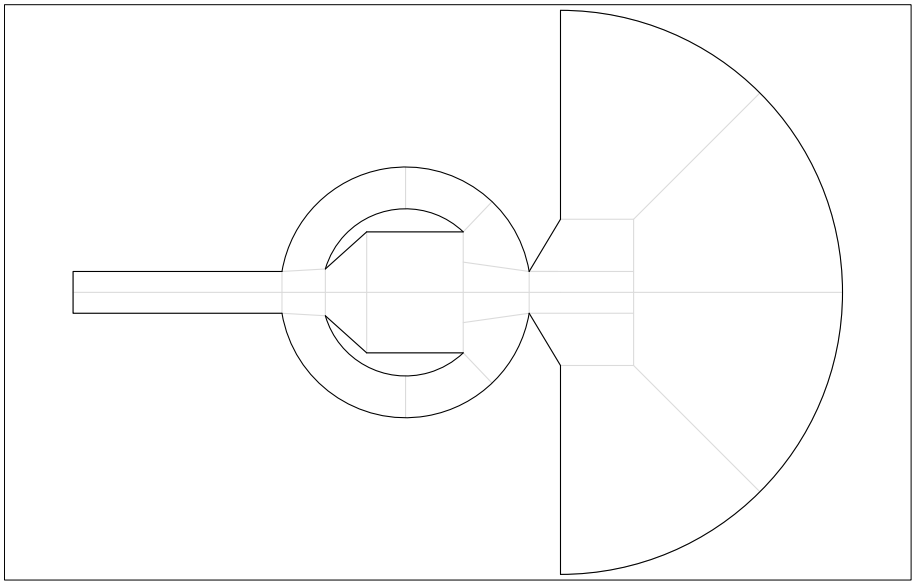

(b)

Figure 9: Sketch of the domain subdivisions of (a) the first and (b) the second designs of the fluidic oscillator. Outer region not to scale.

be seen in Fig. 9, and then lines that connect elements from opposite sides of the domain partitions form the mesh. This is easier for quadrilateral subdivisions, since each pair of opposite sides can be set to have the same number of elements that will then be connected to each other. However, domain subdivisions with more than four sides are also possible, as long as some sides are considered together, resulting in four distinct boundaries which can be connected to their opposite boundary. An example of this kind of subdivision can be seen in the domain divisions between the inner blocks of the fluidic oscillator, whose right sides will be treated as one in order to connect them to their left sides. The same can be seen in the rightmost part of the outer region.

The subdivisions for both designs are identical except from the area between the two inner blocks. In Fig. 9a, corresponding to the first design, it can be seen that there is only one subdivision at each side of the horizontal axis, while in the second design shown in Fig. 9b there are two subdivisions, accounting for the point in which the two inner walls of the inner blocks connect.

The domain subdivisions have been designed so that opposite sides of each partition would be as parallel as possible, in order to avoid cells in the mesh that would be too skewed, which would lead to inaccurate results or problems in the simulation. In order to avoid this, special treatment has been taken in the area between the right vertex of the inner blocks and the outlet nozzle and in the area between outlet nozzle itself and the outer region where, in the early mesh designs, there were opposite sides that were in a very oblique position with respect to one another. This has been solved by setting some domain subdivisions to have five sides, allowing the neighboring subdivision to be split in two.

The connecting of elements from opposite sides of each domain partition has been done in a way that there are more lines near the vertices and walls of the fluidic oscillator, resulting in a finer mesh near these features and a coarser one away from them. The resulting mesh for both designs can be seen in Fig. 10.

The meshes of the fluidic oscillators simulated in this thesis have been created using the software Gmsh which, on exporting the mesh to a file compatible with Nektar++, generates additional nodes in each mesh element depending on the order set for the mesh construction. In this case, the order has been set to five, meaning that, in the final mesh, each element is divided in a grid of 5x5 elements, giving extra accuracy to the simulations.

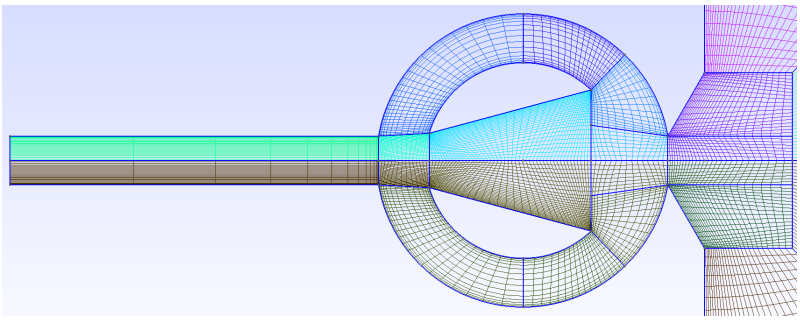

(a)

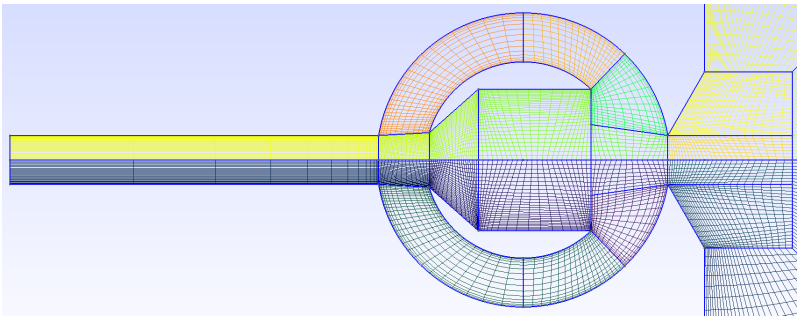

(b)

Figure 10: Close up of the meshes of (a) the first and (b) the second designs of the fluidic oscillator. The mesh in the outer region, not shown in these images, gets coarser as it approaches the outflow boundary, since the flow features are not so important away from the fluidic oscillator.

4.4 Data processing

When running Nektar++ with the specifications set in Sec. 4.2 and the mesh generated following the directions stated in Sec. 4.3, the software iterates the fluid governing equations each time step until the preset final time is reached. However, the information of each time step is not recorded, since that would not be practical to work with in most cases. Therefore, the simulation has been set up so that the solver exports the solution every time unit (i.e. once every 500 steps) in form of a .chk file, which contains all the information about the velocity and pressure fields in every node of the mesh at that specific time.

These files are then converted to .vtu format, which can be visualized using the software Paraview, making it possible to visualize the results as an image or export the values of each variable in any point of interest for the appropriate results.

The exported values, saved in .csv format at first, can then be processed using Matlab to obtain plots that make it easier to visualize the data or to make any needed calculations.

5 Results

In order to measure the oscillatory motion of the fluidic oscillator in the results obtained from the simulations, so that they can be compared between each other, the followed approach has been to set a probe (seen in Figs. 7 and 8) to measure the vertical velocity v for each time unit in the midpoint between the two vertices of the outlet nozzle, which results in an oscillating signal for which the period can be measured and whose amplitude gives a good vision on how pronounced the oscillation of the jet in the outlet is.

The frequency in each simulation has been calculated by taking the inverse of the period, which has been obtained with the following procedure: the time interval between the first local maximum and the last one is divided by the number of complete oscillations between the two. Then, the same is done for the first and last local minima and the two values are averaged.

To compare the frequency at different scenarios and flow rates, a dimensionless frequency, given by the Strouhal number, must be used:

$$St = \frac{fL}{u}\,. \tag{13}$$

However, since the simulation parameters have been set so that $u_{mean} = 1$ and $L = 1$, Eq. (13) becomes

$$St = f\,, \tag{14}$$

the oscillating frequency. As a consequence, the terms Strouhal number and frequency can be used interchangeably in the scope of this thesis, and from now only the term frequency will be used for the sake of simplicity.

To get the amplitude, the absolute values of the vertical velocity at every local extrema have been averaged, in order to get more accurate results.

5.1 Inner blocks choice

First of all, the two fluidic oscillator designs described in Sec. 3.1 need to be compared, in order to determine the differences in the flow inside them and to choose which one performs better, to then study that design in detail.

Four different inner block geometries have been considered, including the first and second design and two designs in between, which can be seen in Fig. 11.

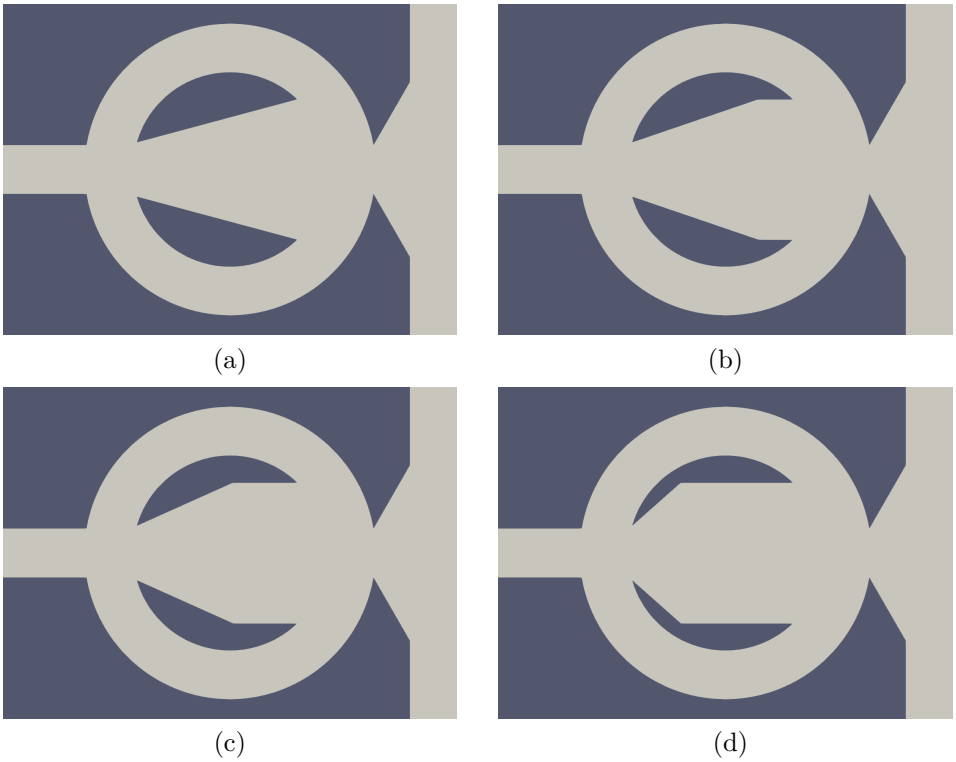

Figure 11: Different geometries of the inner blocks: (a) the first design, (b) design with the vertex between the walls at $\frac{1}{3}$ of the way to the second design, (c) at $\frac{2}{3}$ of the way to the second design and (d) the second design.

The simulations have all been done with the parameters $\theta = \theta_{default}$ and $Re = 250$ for the four different geometries.

The first thing that can be noticed at first sight from the plotted results in Fig. 12 is that the amplitude for the second design is more than double the amplitude for the first design. Also, the frequency appears to be also nearly double in the first design. The values of both the frequency and the amplitude can be seen better in Fig. 13, where they can be more easily compared between each other.

Since the walls at the beginning of the inner blocks are closer to the horizontal in the first design, the Coandă effect has a larger impact on this geometry, so with any little perturbation that pushes the jet away from one wall, the opposite one attracts the jet easily, and therefore the time it takes for the jet to sweep from one side to the other is reduced. However, since the walls are also closer together overall, the jet doesn't deviate very much, resulting in a small amplitude at the outlet nozzle.

On the second design, the jet encounters significantly sloped walls at the beginning of the inner blocks, so the jet can deviate more than in the first one. This is enhanced by the bigger recirculation bubble that arises in the extra space, which pushes the jet further into the opposite side, resulting in a larger amplitude but at the cost of taking more time per oscillation, giving the oscillator a lower frequency.

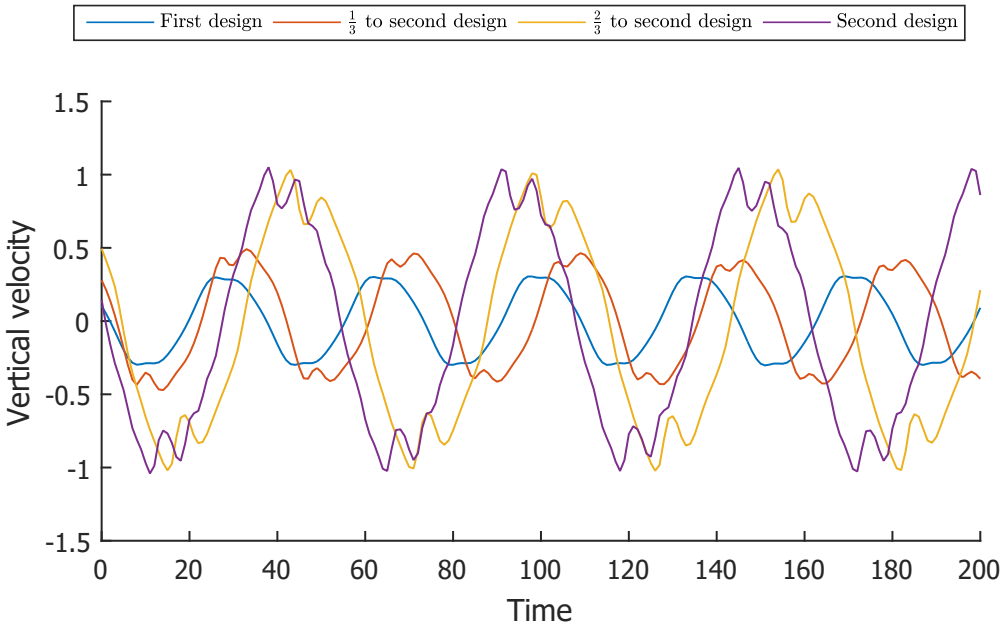

Figure 12: Vertical velocity at the outlet nozzle midpoint for the four different geometries.

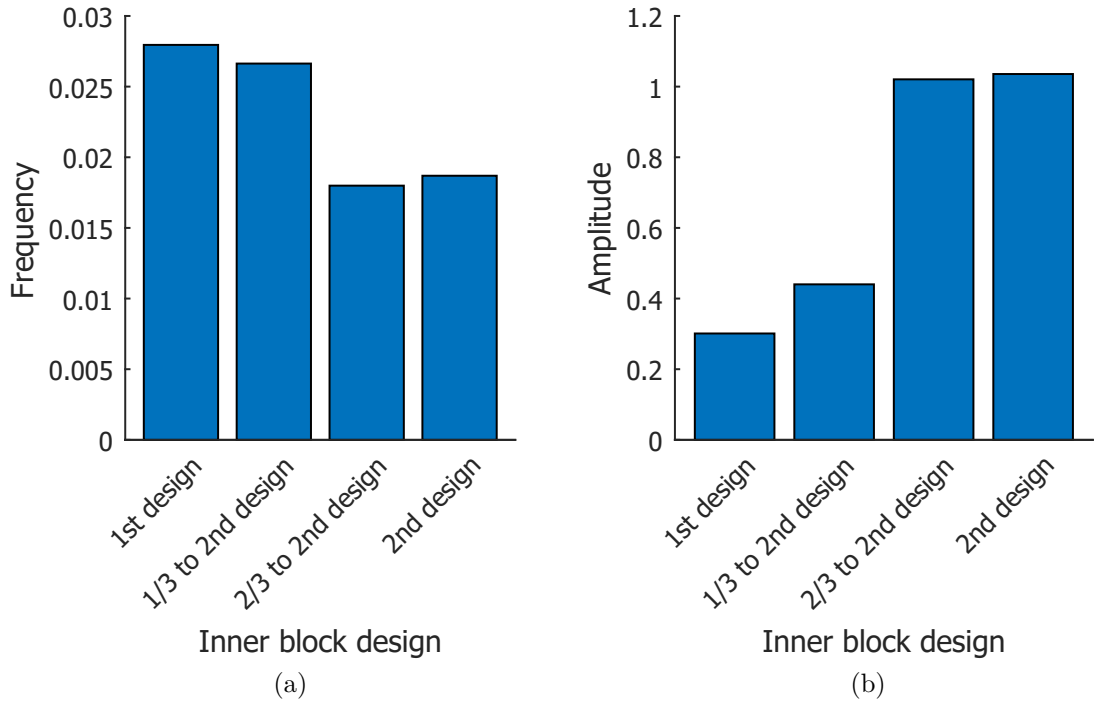

Figure 13: Different values of (a) the frequency and (b) the amplitude for the four different geometries.

Between the two main designs, the amplitude can be seen to cover intermediate values, as expected, while the frequency encounters a minimum point around $\frac{2}{3}$ of the second design geometry. The frequency is then slightly higher in the second design, presumably as a result of the bigger recirculation bubble pushing the jet with more strength.

Given the observed results, the second design will be the one used in the following sections.

5.2 Internal dynamics

With the aid of the various snapshots at different time steps during half a cycle of a simulation using $\theta = \theta_{default}$ and $Re = 250$, in Fig. 14, the internal dynamics of the fluidic oscillator can be explained with much more detail than in Sec. 2.3.

At the beginning of the oscillation ($\phi = 0^o$), the jet is deflected downward to the lower wall, as a consequence of the Coandă effect. However the jet is not fully attached to the wall (it is only completely attached near its end), since the slope at the beginning of the inner wall is very pronounced, so a small recirculation bubble is formed between the main jet and the wall. Meanwhile, the recirculation bubble at the opposite side is near its maximum size.

As the lower pressure area generated by the upper recirculation bubble draws the main jet slightly towards the upper wall, the small recirculation bubble enclosed between the jet and the lower wall begins to grow, pushing the jet a bit more upwards ($\phi = 45^o$). This change in the flow begins to generate a secondary flow around the lower inner block, through the feedback channel, which separates the main jet from the lower wall, easing the upward movement.

Later, while the upper recirculation bubble gets smaller and the lower one bigger, the beginning of the jet continues moving upward and, the part of the jet near the outlet nozzle, which is still near the lower wall, impinges on the fluidic oscillator outer wall, deviating part of its flow through the lower feedback channel input, which in turn helps push the main jet toward the upper wall ($\phi = 90^o$). The impingement can be appreciated in the pressure field, since the pressure in that area increases.

After that, the main jet is near enough to the upper wall so that the Coandă effect pulls it towards the upper wall ($\phi = 135^o$), enclosing the upper recirculation bubble once the jet is attached.

Finally, the upper recirculation bubble reaches its minimum size while the lower one is at its maximum size ($\phi = 180^o$), reaching a situation symmetric to the starting one, so the same mechanism repeats closing the complete oscillation cycle.

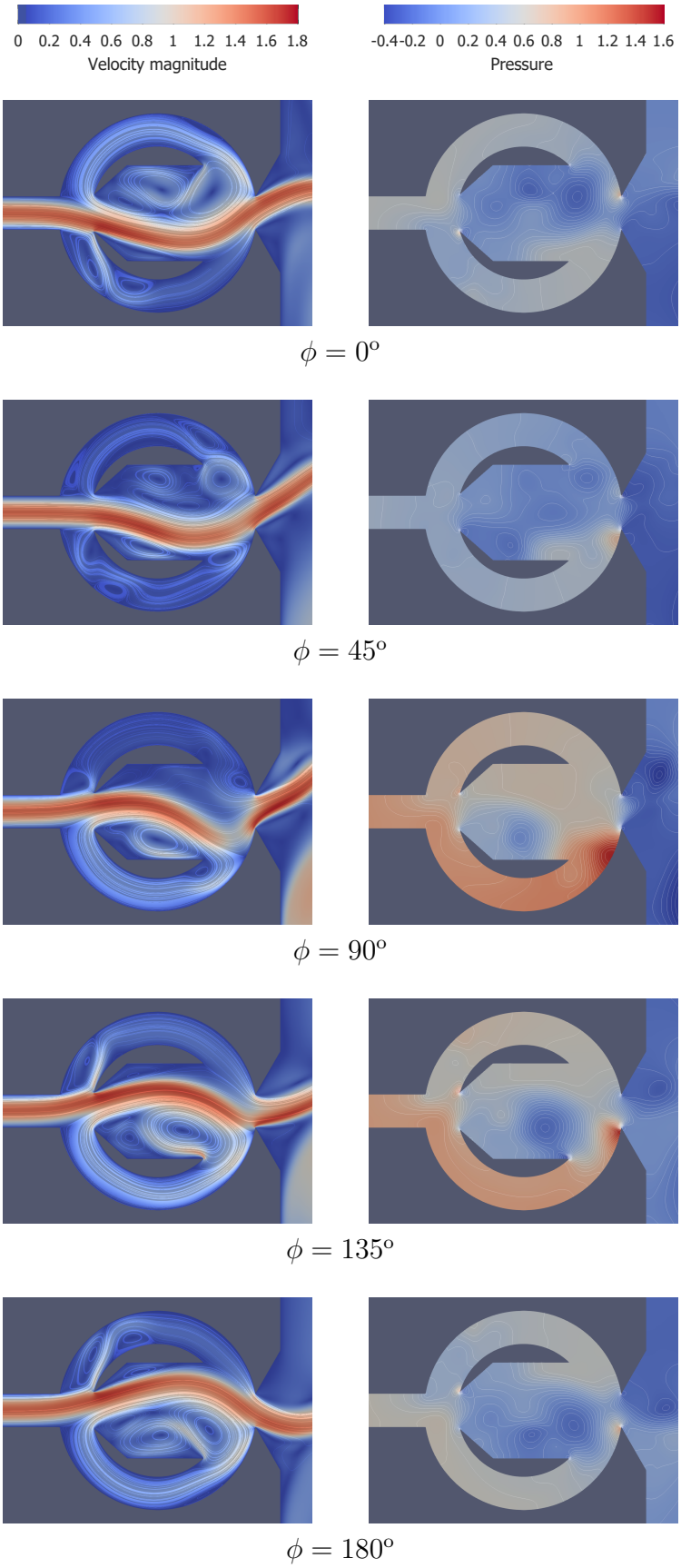

Figure 14: On the left, the internal flow of the oscillator with overlaid streamlines and, on the right, the pressure field with overlaid pressure contours, for different phase angles along a semicycle.

It must be noted that, as can be seen for $\phi = 0^o$, when the jet is fully deflected, a part of the jet enters through the feedback channel output, resulting in a reverse flow that presumably slows down the oscillations, decreasing the frequency. The reason for this is that the adverse flow in the feedback channel should retard the phenomena explained for $\phi = 45^o$, given that this adverse flow must be stopped before the flow from input to output begins[2]. This will be discussed with a bit more detail in Sec. 5.4.

5.3 Influence of the Reynolds number

In order to see the effect of the Reynolds number in the fluidic oscillator, four simulations with the same geometry ($\theta = \theta_{default}$) but different Reynolds numbers have been done. The Reynolds numbers used are $Re = 150$, $Re = 200$, $Re = 250$ and $Re = 300$.

The results, shown in Fig. 15, hint a change in the frequency and show clearly a slight variation in amplitude. These can be seen better in Fig. 16, where the variations are made clear. As expected, the amplitude increases with the Reynolds number, but the frequency behaves opposite of what was expected.

According to most literature, the frequency of the fluidic oscillator increases when the Reynolds number goes up, but the Reynolds values encountered in those articles lay well into the turbulent regime. The Reynolds numbers studied in this thesis are in the laminar regime, so a different correspondence between the two is possible. In fact, at the point the flow reaches the turbulent regime, the oscillating laminar jet is symmetrized by the appearance of turbulence, becoming statistically stationary. Only after increasing the Reynolds number even more would the oscillations take place again. However this cannot be proved in this thesis since turbulent flow has not been treated.

In any case, comparing the simulations of $Re = 150$ and $Re = 300$ with more detail, it can be observed that the adverse flow generated in the feedback channels due to the jet entering through the feedback channel output is stronger and takes longer to dissipate for $Re = 300$ than for $Re = 150$, which can explain that the frequency at increasing Reynolds number is lower.

Besides, the dependency of both the amplitude and frequency with respect to the Reynolds number doesn't appear to be linear, as the literature suggests.

[2]Note that, in the feedback channels, forward flow is considered to go from right to left, since that's the direction for which motion is expected in order for the fluidic oscillator to function.

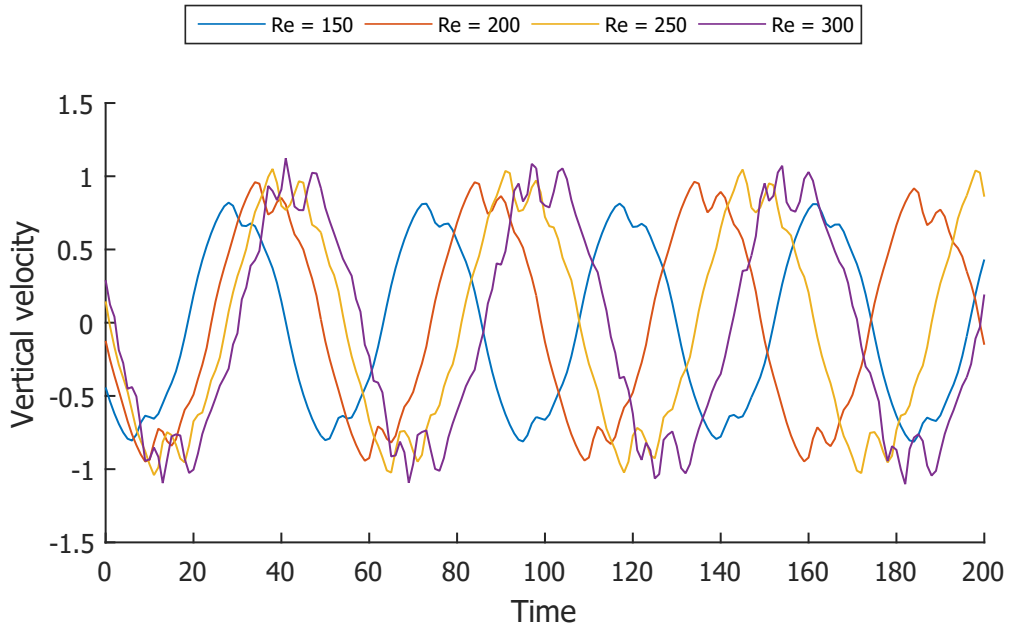

Figure 15: Vertical velocity at the outlet nozzle midpoint for different Reynolds numbers.

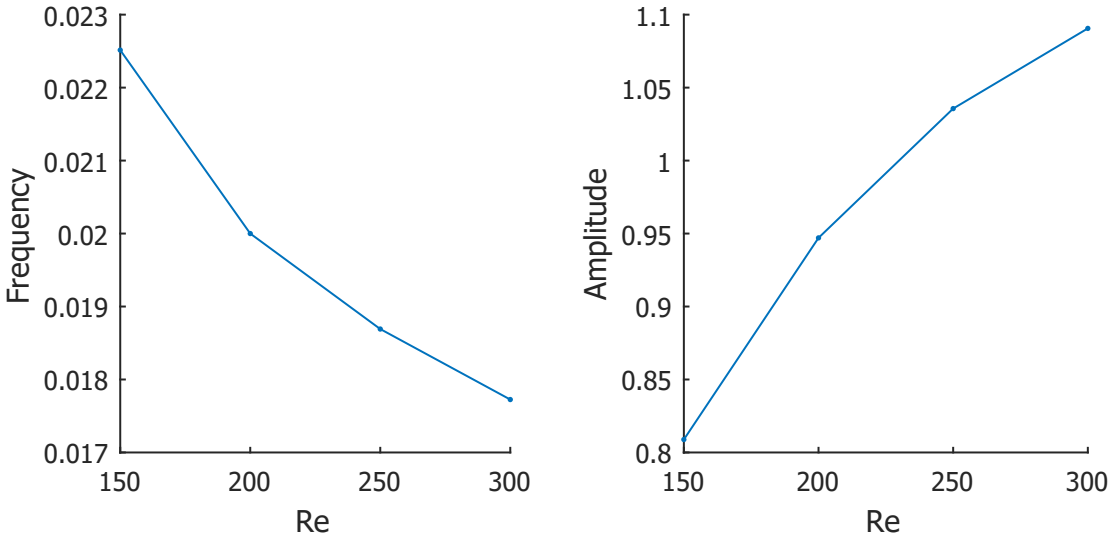

(a) (b)

Figure 16: Variation of (a) the frequency and (b) the amplitude in function of the Reynolds number.

5.4 Effects of changes in the geometry

As stated before in Sec. 3 and demonstrated in the previous section, changing the Reynolds number modifies both the oscillation frequency and the amplitude. However, in order to ultimately decouple these two parameters, another way of modifying them is required.

Since the fluidic oscillator works due to its geometry, any change in it should modify the output flow. To change it, the angular position of the inner blocks θ can be tweaked and, since this doesn't deform any piece of the fluidic oscillator, the angle θ could be adjusted in mid operation by the means of mechanical actuators.

To study this effect, four different main angular positions have been studied, being $\theta = \frac{\pi}{18}$, $\theta = 1.25 \cdot \frac{\pi}{18}$, $\theta = 1.5 \cdot \frac{\pi}{18}$ and $\theta = 1.75 \cdot \frac{\pi}{18}$, and an additional one at $\theta = 1.62 \cdot \frac{\pi}{18}$ in order to examine the transition between the two very different behaviors between $\theta = 1.5 \cdot \frac{\pi}{18}$ and $\theta = 1.75 \cdot \frac{\pi}{18}$. The geometries can be seen in Fig. 17.

In all these cases, the default angular position has been set to $\theta_{default} = 1.5 \cdot \frac{\pi}{18}$, as in the rest of simulations, meaning that at that angle the right wall of the inner blocks is parallel to the horizontal axis, while at lower angles it has a negative slope and, at higher angles, a positive one. It must be noted that on rotating the inner blocks the entrance to the mixing chamber constricts or expands, depending on their angular position.

As can be seen in Fig. 18, the results from $\theta = \frac{\pi}{18}$ to $\theta = 1.5 \cdot \frac{\pi}{18}$ are quite similar, with apparent variations in amplitude and frequency but the results for $\theta = 1.75 \cdot \frac{\pi}{18}$ differ much from the rest. The signal at that angle presents a much higher frequency and a significantly lower amplitude. In order to see better the transition in this sudden change, the extra simulation at $\theta = 1.62 \cdot \frac{\pi}{18}$ has been done.

Showing the measured frequencies and amplitudes, in Fig. 19, shows that the behavior between $\theta = \frac{\pi}{18}$ and $\theta = 1.5 \cdot \frac{\pi}{18}$ can be considered linear, but after that the linearity is lost and both parameters change abruptly.

Analyzing in detail the simulations, it can be seen that for $\theta = 1.75 \cdot \frac{\pi}{18}$ the initial slope of the inner blocks is too high, so the Coandă effect cannot pull the jet all the way to the second wall of the blocks. As a result, the oscillations are way smaller, as seen in the decrease in amplitude, and therefore the jet takes less time to travel from one side to the other, resulting in a higher frequency. Even though the Coandă effect is very weak at this angle, the oscillation is still maintained by the interaction of the jet and the flow in the feedback channels and the recirculation bubbles. This effect also happens for $\theta = 1.62 \cdot \frac{\pi}{18}$ but not as prominent.

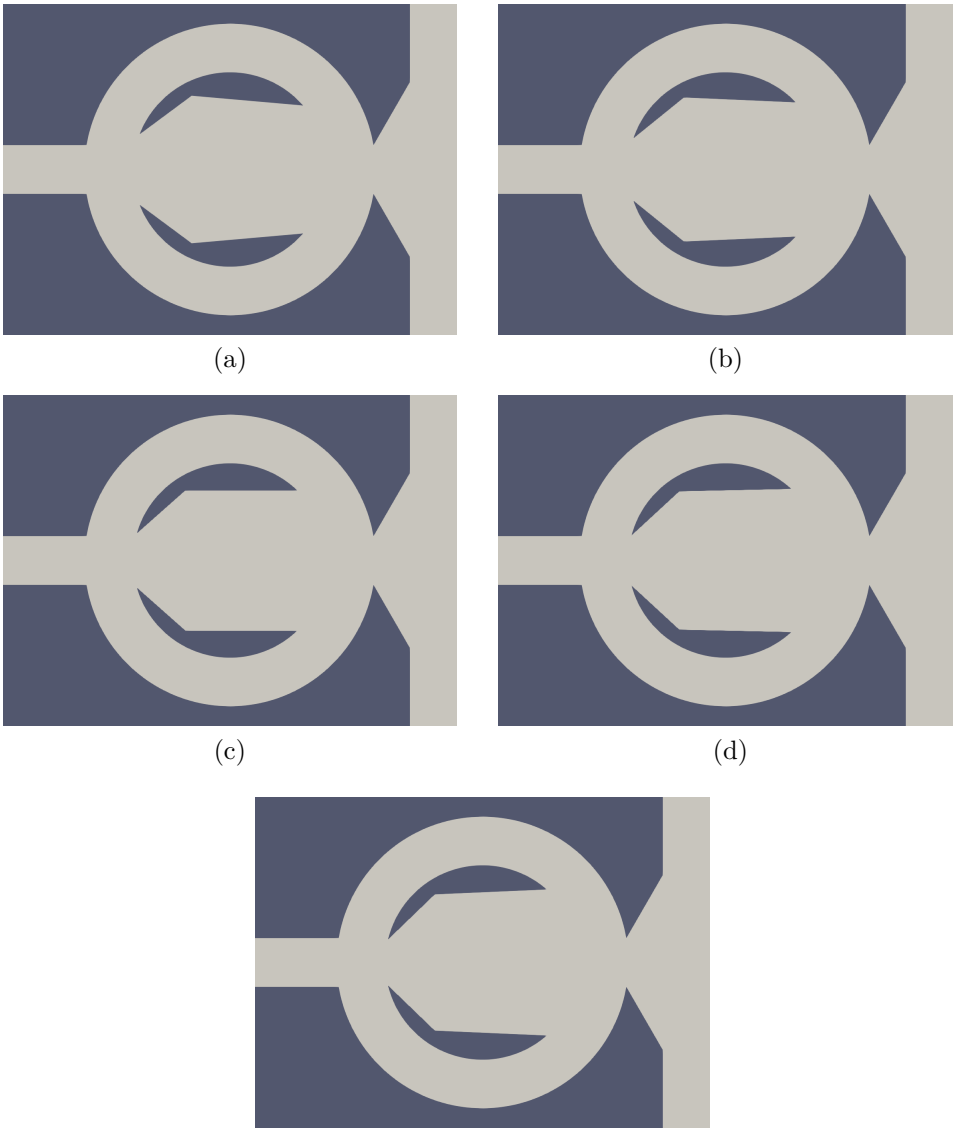

Figure 17: Inner blocks with different angular positions, at (a) $\theta = \frac{\pi}{18}$, (b) $\theta = 1.25 \cdot \frac{\pi}{18}$, (c) $\theta = 1.5 \cdot \frac{\pi}{18}$, (d) $\theta = 1.62 \cdot \frac{\pi}{18}$ and (e) $\theta = 1.75 \cdot \frac{\pi}{18}$.

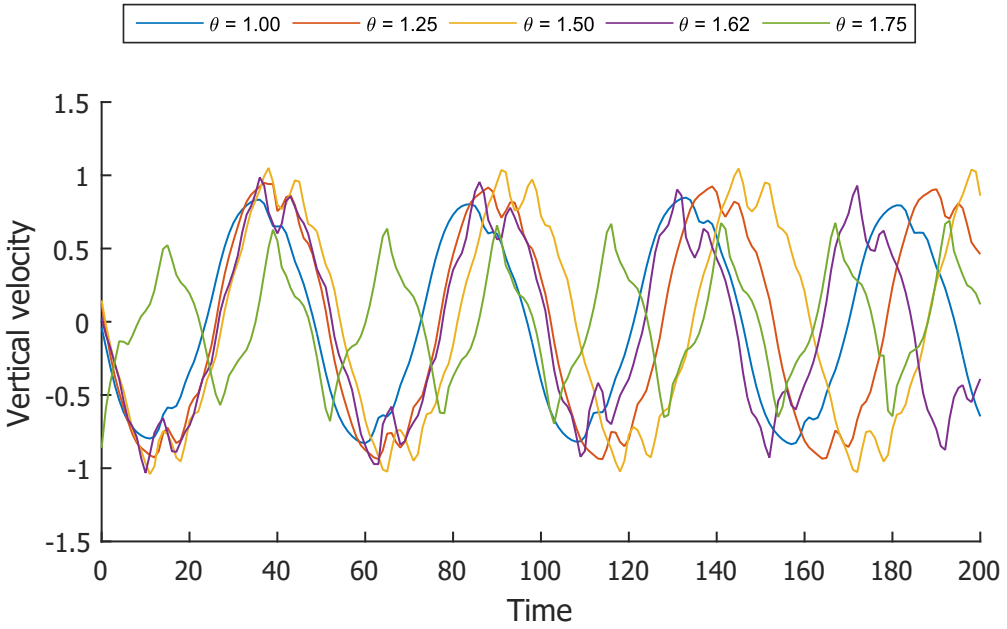

Figure 18: Vertical velocity at the outlet nozzle midpoint for different angles θ. All values in the legend are multiplied by a factor $\frac{\pi}{18}$.

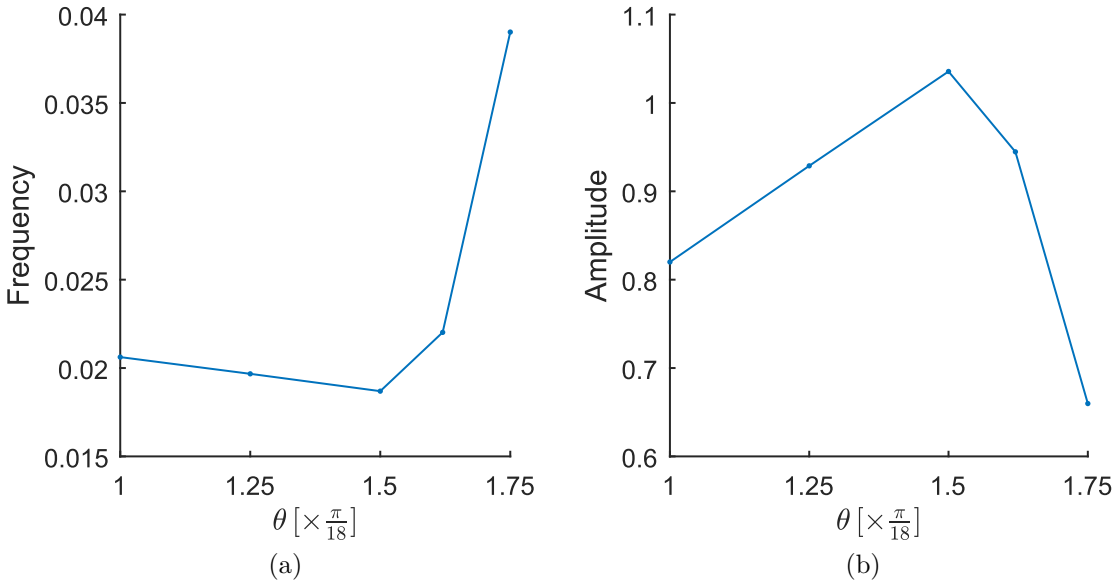

Figure 19: Variation of (a) the frequency and (b) the amplitude in function of the angle θ.

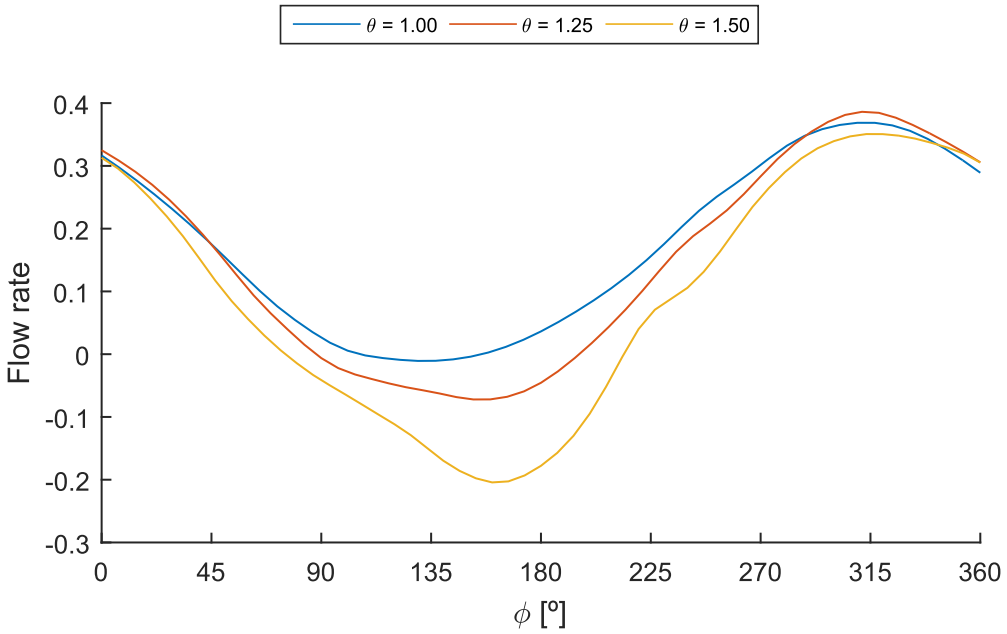

Figure 20: Flow rate across the upper feedback channel for different angles θ. Positive values represent flow from right to left. All values in the legend are multiplied by a factor $\frac{\pi}{18}$.

As a consequence of the observed behavior at $\theta > \theta_{default}$, the subsequent simulations will only be performed at $\theta \leq \theta_{default}$, between the values $\theta = \frac{\pi}{18}$ and $\theta = 1.5 \cdot \frac{\pi}{18}$.

It's interesting to see that, when decreasing the angle θ, since the mixing chamber entrance expands, the adverse flow in the feedback channels observed in Sec. 5.2 is reduced, as can be observed in Fig. 20. The maximum adverse flow rate[3] happens between $\phi = 135^{\circ}$ and $\phi = 180^{\circ}$, as could be appreciated previously in Fig. 14, but it gets much smaller as the angle decreases, since less fluid from the inlet nozzle can enter directly the feedback channels.

5.5 Amplitude-frequency decoupling

In order to finally determine if it's possible to decouple the amplitude and the frequency, several combinations of Reynolds number and angular configuration of the inner blocks must be tested, to provide enough information on how the two parameters react when both variables are changed.

The study has been performed using the fluidic oscillator in various angular configurations ranging from $\theta = \frac{\pi}{18}$ to $\theta = 1.5 \cdot \frac{\pi}{18}$, in intervals of $\Delta\theta = 0.1 \cdot \frac{\pi}{18}$, and the Reynolds numbers already studied between $Re = 150$ and $Re = 300$, in intervals of $\Delta Re = 50$. All the resulting simulation results can be seen in Fig. 21.

[3]The flow rate used here represents the two-dimensional volumetric flow rate, given by $Q = \int_{CS} u \cdot dl$, where CS is the cross section of the feedback channel.

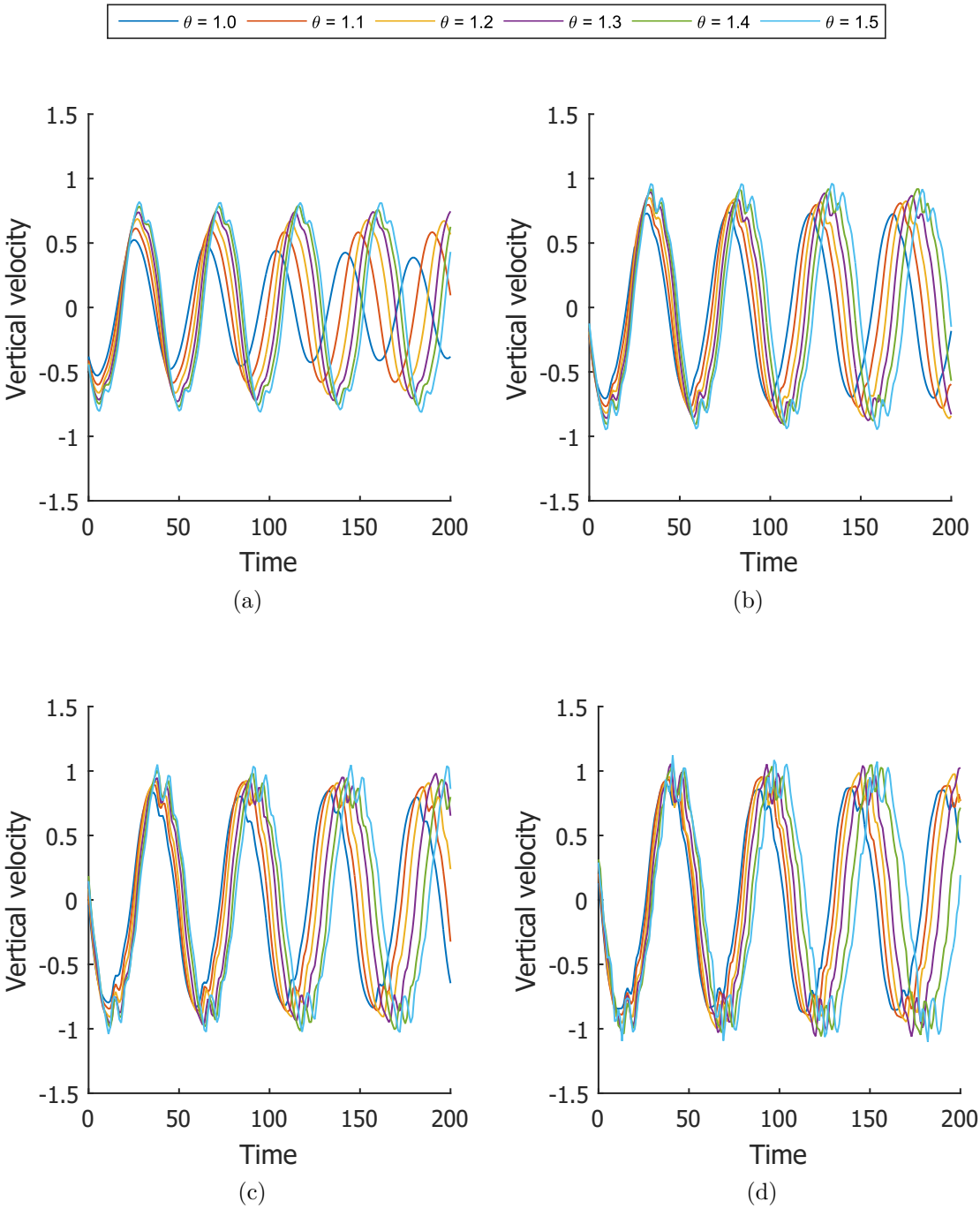

Figure 21: Vertical velocity at the outlet nozzle midpoint for different angles θ at (a) $Re = 150$, (b) $Re = 200$, (c) $Re = 250$ and (d) $Re = 300$. All values in the legend are multiplied by a factor $\frac{\pi}{18}$.

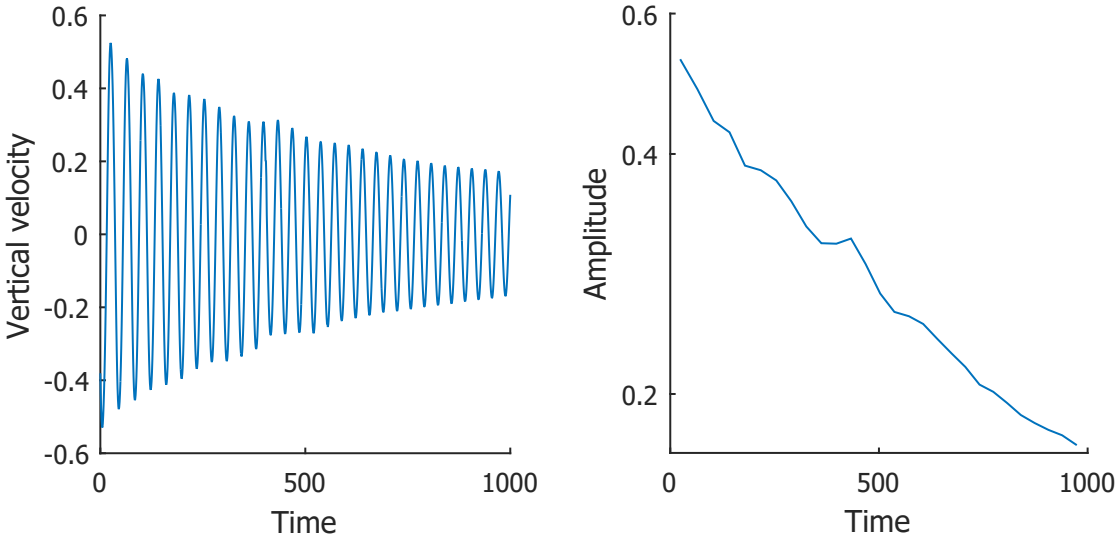

Figure 22: (a) Vertical velocity at the outlet nozzle midpoint for $\theta = \frac{\pi}{18}$ at $Re = 150$ and (b) semilogarithmic plot of the amplitude.

While most of the plots in Fig. 21 look as expected compared to the results compiled in Sec. 5.4, the simulation at $Re = 150$ and $\theta = \frac{\pi}{18}$ (dark blue line in Fig. 21a) stands out from the rest, since the amplitude seems to decrease over time. The simulation for those values has been extended in order to determine if the decreasing trend in the amplitude is temporary, due to transitory effects, or an actual consequence of the Reynolds number and geometry.

As can be seen in Fig. 22, where the simulation time has been extended from 200 to 1000 time units, the amplitude of the signal decreases over time close to an exponential manner, meaning that over time the oscillation would disappear. The reason for this, after a careful examination of the simulation, has been determined to be that, even though the initial angle of the inner blocks walls is very shallow, the vertices that form the mixing chamber entrance are very far apart, so the fluid doesn't attach to the walls easily, and therefore it loses a little bit of vertical displacement in each oscillation. This doesn't happen at higher Reynolds numbers since the resistance to movement is lower as the Reynolds goes up[4].

In Fig. 23, the dependence of the frequency and the amplitude with respect to the inner blocks position at the various Reynolds numbers can be seen and, in Fig. 24, the dependence with respect to the Reynolds number at the different angles θ can be appreciated. It must be noted that the value used for the amplitude at $Re = 150$ and $\theta = \frac{\pi}{18}$ correspond only to the first oscillation and can't be considered reliable,

[4]Increasing the Reynolds number is equivalent to decreasing the kinematic viscosity, as can be seen in Eq. (7).

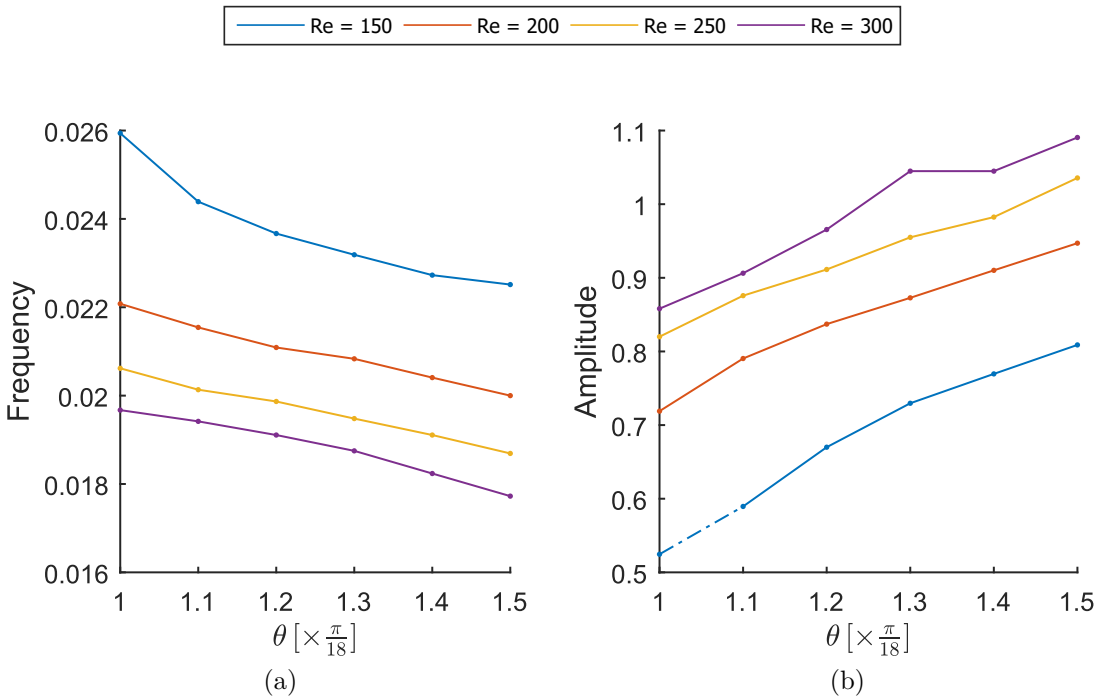

(a) (b)

Figure 23: Variation of (a) the frequency and (b) the amplitude in function of the angle θ, for different Reynolds numbers. The value of the amplitude for $\theta = \frac{\pi}{18}$ at $Re = 150$ cannot be considered reliable, hence the dotted line.

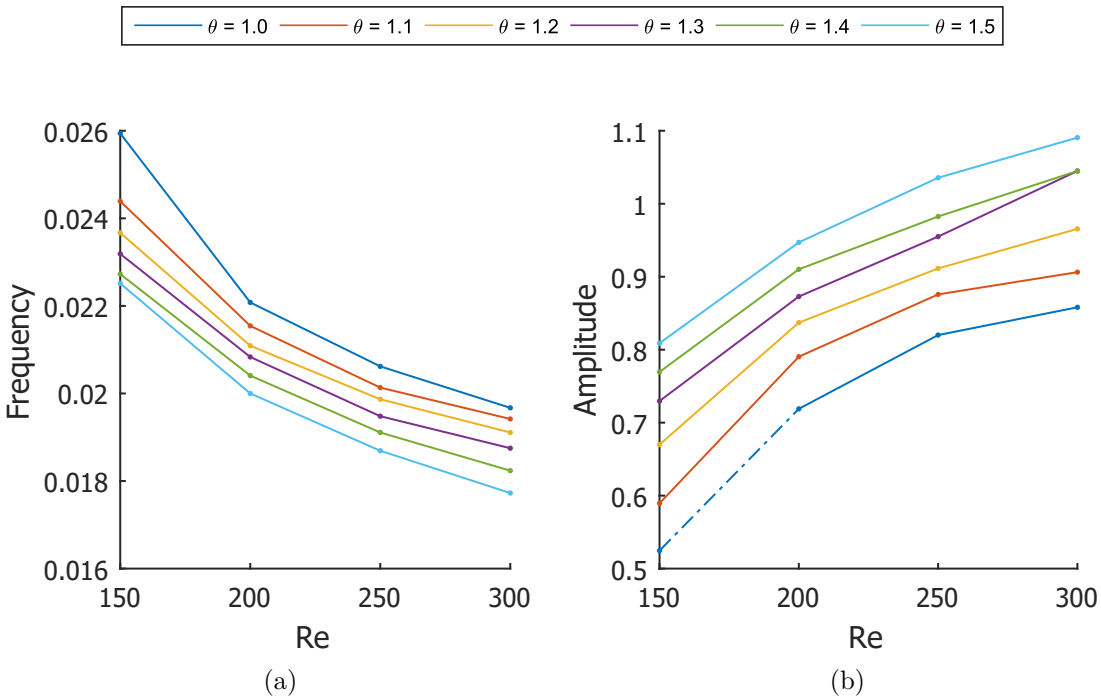

(a) (b)

Figure 24: Variation of (a) the frequency and (b) the amplitude in function of the Reynolds number, for different angles θ. All values in the legend are multiplied by a factor $\frac{\pi}{18}$. The value of the amplitude for $\theta = \frac{\pi}{18}$ at $Re = 150$ cannot be considered reliable, hence the dotted line.

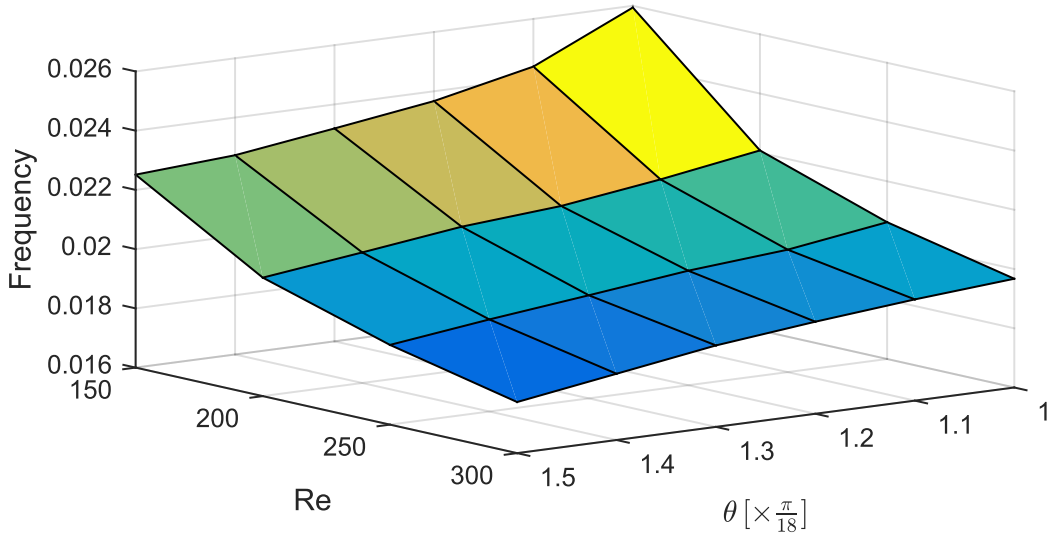

(a)

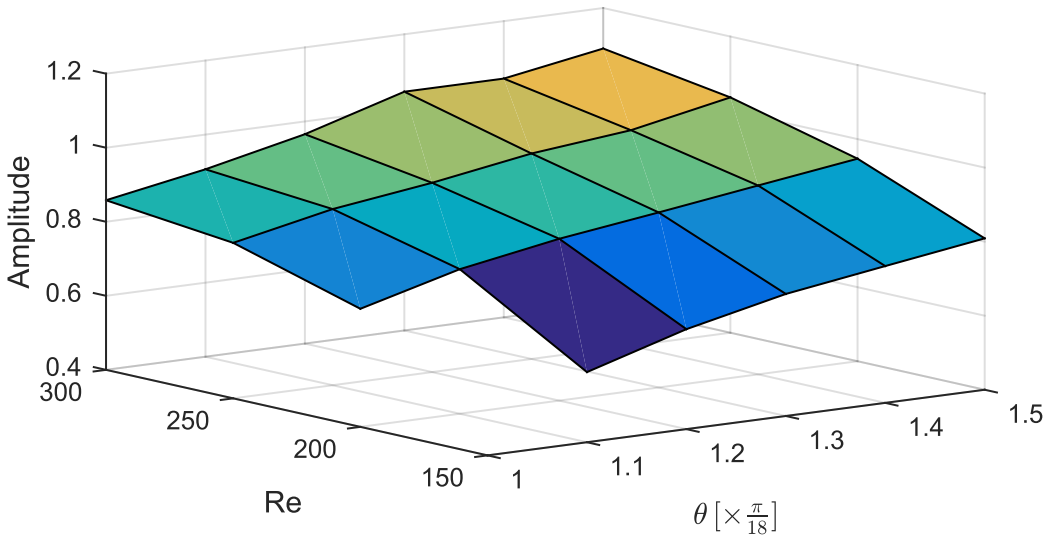

(b)

Figure 25: Two-dimensional plots representing the dependence of (a) the frequency and (b) the amplitude with respect to both the Reynolds number and the angle θ.

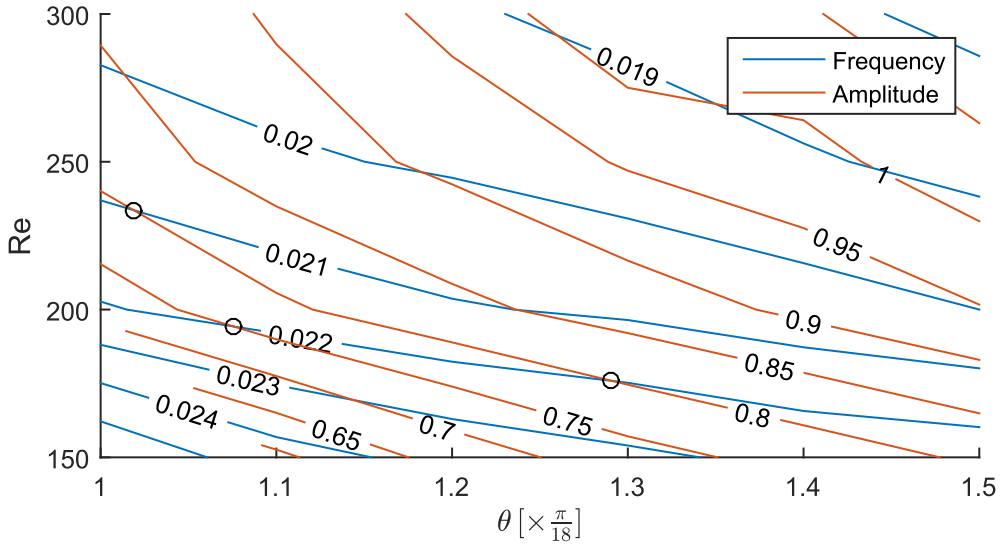

Figure 26: Contour lines for both the frequency and the amplitude showing the θ-Re pair paths in which each is constant. The region without amplitude contours is due to the unreliability of the amplitude measurement at $\theta = \frac{\pi}{18}$ and $Re = 150$. The black circles can be used for exemplary purposes.

since the amplitude decreases over time, so it has been marked with a dotted line. As a result, this value will be omitted in the upcoming plots.

The same data can be seen put together in Fig. 25, where it can be seen clearly that decreasing either the Reynolds number or the angle θ the frequency increases and the amplitude decreases, and the opposite happens if they are increased. It also becomes more apparent that the frequency and the amplitude can be set, within a certain values, independently from each other by tweaking the orientation of the inner blocks and changing the Reynolds number.

However, to see that more clearly, the best strategy is to plot the contours across a θ-Re field in which the values of the amplitude are the same, and the same for the frequency. This representation can be seen in Fig. 26.

An example of the independence of the frequency and the amplitude can be seen using the black circles in Fig. 26. At $\theta = 1.29 \cdot \frac{\pi}{18}$ and $Re = 176$, the amplitude takes a value of $v_{max} = 0.8$ and the frequency of $f = 0.022$. If the requirements call for a lower frequency while maintaining the same amplitude, the parameters can be changed to $\theta = 1.02 \cdot \frac{\pi}{18}$ and $Re = 234$ so that the frequency becomes $f = 0.021$ without changing the amplitude. A similar thing can be done if a lower amplitude is required while keeping the same oscillation frequency: the parameters must be changed to $\theta = 1.08 \cdot \frac{\pi}{18}$ and $Re = 194$ and the amplitude becomes $v_{max} = 0.75$, with the frequency maintaining its former value.

6 Conclusions

Along the course of this thesis several things have been observed. Some of them must be highlighted, since they are relevant to the objectives set in the introduction.

First of all, it should be remarked that both design simplifications of the fluidic oscillator work, since they turn a pressurized jet into an oscillatory one effectively. However, it has been proven that the second design, with the inner blocks resembling more the original design, performs much better than the overly simplified first design which, even though it works, results in oscillations much weaker in amplitude due to the decrease in space in the mixing chamber that leads to smaller recirculation bubbles and less deviation of the jet.

Also, it has been shown that the equivalence between the Reynolds number and the frequency is reversed compared to that encountered in the turbulent regime.

Regarding the fact that the inner blocks of the new design can be rotated around the center of the fluidic oscillator, it has been shown that this feature can be used effectively to modify the frequency and the amplitude at any fixed Reynolds number.

When changing both the Reynolds number and the angle θ, it has been proven possible to change the frequency and the amplitude independently from each other. However, since the contours of both parameters are at a low angle between each other, it's difficult to change one variable considerably and keep the other constant, needing very large changes in the Reynolds number and positioning of the inner blocks in these occasions. This is expected to become easier when using the fluidic oscillator in the turbulent regime, since the dependence between the Reynolds number and the frequency is reversed. If in that situation the frequency keeps decreasing when the angle θ increases, the frequency contours will become much closer to being perpendicular to the amplitude contours. In that case, the frequency and amplitude could be changed independently in a more drastic manner without changes too big in the orientation of the inner blocks and the Reynolds number. Supplementary research could be performed to study the independence of the frequency and the amplitude in the turbulent regime for this design of fluidic oscillator.

In any case, the extent of usable angles of operation and Reynolds numbers should be identified in order to know the operational range of this fluidic oscillator design. Only two values off limits have been found as a result of the experiments performed in this thesis: the decline of the oscillations at both low Reynolds number and angle θ (such as the case for $Re = 150$ and $\theta = \frac{\pi}{18}$) and the performance loss at angles higher than the default position of the inner blocks ($\theta > \theta_{default} = 1.5 \cdot \frac{\pi}{18}$). Apart from those off limit values, it's possible that there will also be issues at

higher Reynolds numbers but lower values of θ, and at lower Reynolds yet higher angles. Also, angles of the inner blocks too small will result in the mixing chamber output being too constricted, which will also probably dissipate the oscillations. Additionally, if the Reynolds number is increased too much, the flow may enter the turbulent regime, presumably losing the laminar oscillations until an even higher critical Reynolds number, where the oscillations would appear again.

Additional research could be done in order to fully determine the operational boundaries of this design of the fluidic oscillator, taking into consideration the observations made above.

Finally, since this study has been done for a two-dimensional fluidic oscillator, it could be extended by investigating the behavior of a fluidic oscillator with this design but in three dimensions, where the width of the device could affect the different results that have been obtained in this text.

References

[1] Arendt, W., and Warma, M.: Dirichlet and Neumann boundary conditions: What is in between?. *Nonlinear Evolution Equations and Related Topics, Birkhäuser Basel* (2003)

[2] Busch, M: Vortex Generators: Band-Aids or Magic?. *Aviation Publishing Group (website)* (1997)

[3] Cattafesta, L. N., III, and Sheplak, M.: Actuators for Active Flow Control. *Annual Review of Fluid Mechanics, vol. 43* (2011)

[4] Dearing, S., Lambert, S., and Morrison, J.: Flow control with active dimples. *The Aeronautical Journal, vol. 111* (2007)

[5] Dong, S.: A convective-like energy-stable open boundary condition for simulations of incompressible flows. *Journal of Computational Physics, vol. 302* (1981)

[6] Erfani, R., Zare-Behtash, H., Hale, C., and Kontis, K.: Development of DBD plasma actuators: The double encapsulated electrode. *Acta Astronautica, vol. 109* (2015)

[7] Gaertlein, S., Woszidlo, R., Ostermann, F., Nayeri, C., and Paschereit, C. O.: The Time-Resolved Internal and External Flow Field Properties of a Fluidic Oscillator. *52nd Aerospace Sciences Meeting, American Institute of Aeronautics and Astronautics* (2014)

[8] Greenblatt, D., and Wygnanski, I. J.: The control of flow separation by periodic excitation. *Progress in Aerospace Sciences, vol. 36* (2000)

[9] Gregory, J., and Tomac, M. N.: A Review of Fluidic Oscillator Development and Application for Flow Control. *43rd Fluid Dynamics Conference, American Institute of Aeronautics and Astronautics* (2013)

[10] Moghaddam, T., and Neishabouri, N. B.: On the Active and Passive Flow Separation Control Techniques over Airfoils. *IOP Conference Series: Materials Science and Engineering, vol. 248* (2017)

[11] Munson B. R., Young D. F., Okiishi T. H. and Huebsch W. W.: Fundamentals of Fluid Mechanics (6th ed.). *John Wiley & Sons* (2009)

[12] Schlichting, H.: Boundary-Layer Theory (7th ed.). *McGraw-Hill Series in Mechanical Engineering* (1979)

[13] Sieber, M., Ostermann, F., Woszidlo, R., Oberleithner, K., and Paschereit, C. O.: Lagrangian coherent structures in the flow field of a fluidic oscillator. *68th Annual Meeting of the APS Division of Fluid Dynamics - Gallery of Fluid Motion, American Physical Society* (2015)

[14] Tritton, D. J.: Physical Fluid Dynamics (2nd ed.). *Oxford Science Publications* (1988)

[15] Woszidlo, R., Ostermann, F., Nayeri, C. N., and Paschereit, C. O.: The time-resolved natural flow field of a fluidic oscillator. *Experiments in Fluids, vol. 56* (2015)

[16] How do Micro VGs Work. *Micro AeroDynamics Inc (website)* (2018)

[17] Nektar++: Spectral/hp Element Framework: User Guide (version 4.4.1). *Department of Aeronautics, Imperial College London, UK &* Scientific Computing and Imaging Institute, University of Utah, USA (2017)

[18] Photograph of a airfoil in a wind tunnel, showing separated flow over the top surface. *Deutsches Zentrum für Luft- und Raumfahrt (extracted via Wikipedia Commons)* (1915)